UNIVERSITÁ DEGLI STUDI DI MILANO
Facoltá di Scienze Matematiche, Fisiche e Naturali
&
UNIVERSITÁ CATTOLICA DEL SACRO CUORE
Facoltá di Scienze Matematiche, Fisiche e Naturali

Doctorate school in Physics, Astrophysics and Applied Physics

Investigation of Electronic and Magnetic properties of Mn-doped Ge(111) and ϵ-GaSe(0001) Surfaces

Settore scientifico disciplinare FIS/03

Coordinator: Prof. Marco Bersanelli
Tutor: Prof. Luigi Sangaletti

Thesis for Degree of Doctor of Philosophy
Sibashisa Dash
Cycle XXIV

Accademic year 2010-2011

Contents

Chapter 1

Introduction

1.1 Diluted magnetic semiconductors and spintronics

Spintronics appeared from the very beginning as a very promising way to improve electronic devices. However, while significant breakthroughs have been made, its full potential is still to be achieved. The bottleneck is the lack of suitable materials allowing simultaneous control over electric and magnetic properties.

Ferromagnetism and semiconducting properties are known to coexist in magnetic semiconductors, such as europium chalcogenides and semiconducting spinels that have a periodic array of magnetic elements. However, the crystal structure of such magnetic semiconductors is quite different from that of Si and GaAs, which may lead to a poor lattice matching hampering the fabrication of robust devices. In addition, the crystal growth of these compounds is notoriously difficult. To obtain even a small, single crystal requires weeks of preparation and growth.

Diluted magnetic semiconductors (DMS) represent a new class of material which combines both the charge and spin of the electron. In todays technologies, two degrees of freedom of electrons, charge and spin, can be well handled and applied to practical devices but separately. Integrated circuits used for data processing utilize the charge degree of freedom of electrons in semiconductors while data storage media utilize the spin degree of freedom of electrons in magnetic materials. With remarkable developments of each technology, new technology has started to emerge recently. The technology is called spin-electronics or spintronics in which both the charge and spin degree of freedoms of electron are utilized simultaneously. Combination of the properties related to the charge and the spin of electrons will substantially increase the capabilities of electronics. The injection of spins into nonmagnetic semiconductors has recently attracted great interest due to the possibilities to create classes of spin-dependent electronic devices. In order to inject spin-polarized currents into nonmagnetic semiconductors, many groups have tried to use ferromagnetic (FM) metals i.e., Fe as spin sources, forming metal-semiconductor heterostructures. However, the spin orientation of the carriers tends to be quickly lost at a ferromagnet-semiconductor interface via spin-flip scattering due to the dissimilar crystal structure and chemical bonding, and the energy difference between the charge carriers in the ferromagnet and the semiconductor(1). A more promising strategy to achieve spin injection into nonmagnetic semiconductors is to use a diluted ferromagnetic semiconductor (DFS), prepared by substituting magnetic ions such as Cr^{2+}, Mn^{2+}, Co^{2+}, Ni^{2+}, and Fe^{2+} into nonmagnetic semiconductors.

For practical applications, one needs to find diluted ferromagnetic semiconductors, which have T_C above room temperature and can be easily n-type or p-type doped. The topic has become more important for pursuing high quality system with higher Curie temperature as after the report on making nonmagnetic semiconductor to ferromagnetic by H. Ohno(3) on a III-V Semiconductor system. Fig.1.1(2) shows the predicted values of the Curie temperature T_c for several III-V, group IV, and II-VI semiconductors containing 5 % of Mn in the cation sublattice and a carrier density of 3.5 x 10^{20} holes per cm^3. Up to date many of them have been explored, though predictions have not always been confirmed both in terms of ferromagnetism and Curie temperatures. Others have been added in the recent years, those based on Mn-Ge being still extensively studied, and new ones being currently under test, such as compounds the III-VI binary compounds.

However, device applications have often languished because of low magnetic ordering (Curie) temperatures and the inability to incorporate these materials in thin film form with mainstream semiconductor device materials.

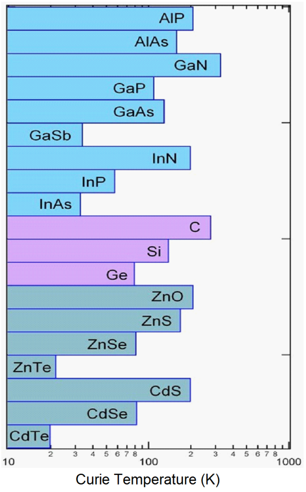

Figure 1.1: Curie temperatures predicted for various III-V, group IV and II-VI semiconducting compounds containing 5 % of Mn per cation in a +2 charge state and 3.5×10^{20} holes$\cdot$ cm^{-3} (from ref.(2)).

1.2 The Mn-Ge system: bulk DMS, interfaces, and devices.

Since the discovery of ferromagnetism in the Mn_xGe_{1-x} diluted magnetic semiconductor (DMS)(6), the Mn-Ge system has played a central role for possible applications in the field of spintronics. Indeed, the Mn-Ge system has shown to be a very rich playground for testing spintronic architectures, ranging from the Mn_xGe_{1-x} diluted alloy (x=0.01 to 0.05)(6) in which the curie temperature is found to increase linearly with manganese (Mn) concentration from 25 to 116 K as shown in the Fig.1.2, to a number of Mn:Ge(100)(9), Mn:Ge(111) interfaces(10,11,12) or amorphous, ferromagnetic, Mn-Ge thin films(13).

Recently, device based on nanostructured DMS, a system with $Mn_{0.05}Ge_{0.95}$ quantum dots (QDs) has been reported (Fig. 1.3, from Ref.(5)) with a Curie temperature T_c above 300 K. This system represents a successful demonstration of electric-field control of ferromagnetism by using quantum size effects, showing that high-quality materials can be obtained and an effective hole mediation due to quantum confinement effects achieved. Upon the application of gate bias to a metal-oxide semiconductor (MOS) capacitor, the

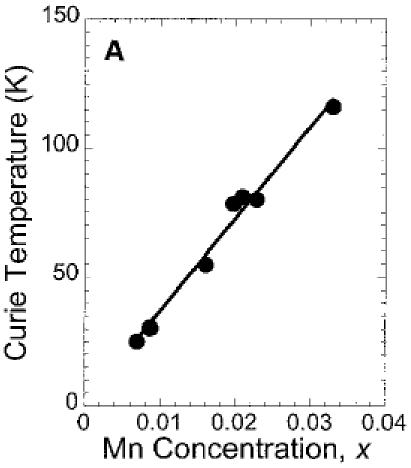

Figure 1.2: Dependence of T_c on the Mn concentration of the FM Mn_xGe_{1-x} matrix from ref.$^{(6)}$.

ferromagnetism of the channel layer, that is, the $Mn_{0.05}Ge_{0.95}$ quantum dots, was manipulated through the change of hole concentration. The results are fundamentally and technologically important toward the realization of room-temperature spin field-effect transistors and nonvolatile spin logic devices.

When dealing with DMS, during the sample growth it is likely to find the presence of segregated phases and clusterized defects, depending on the amount of Mn and the growth temperature. There are different possible precipitates/phases of Mn-Ge system grown in different thermodynamic conditions; for example 16 different structural phases are known, depending on Mn ion concentration as shown in Fig.1.4 starting with those stable in standard conditions, then high-temperature compounds and finally high-pressure compounds$^{(4)}$. These phases may be found either as segregations or constitute themselves FM systems to be coupled to a Ge substrate or to be grown inside the bulk of a Ge host crystal.

The possible crystalline phases in the Mn-Ge system have been computationally explored in a recent theoretical study$^{(4)}$ by using projector augmented-wave (PAW) method as implemented in the ABINIT code within the generalized gradient approximation (GGA). All these compounds and their properties, starting with those stable in standard conditions, then high-temperature compounds and finally high-pressure compounds are shown in the figure 1.4 from ref.$^{(4)}$. The magnetic phases of these compounds have

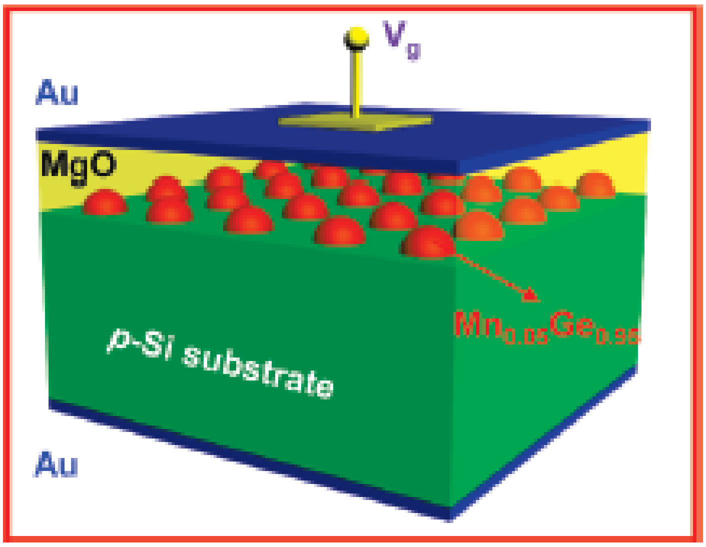

Figure 1.3: A schematic drawing of a MOS capacitor, consisting of electrodes (Au), MgO, $Mn_{0.05}Ge_{0.95}$ QDs, and p-type Si substrate. Note that there is a thin Mn_xGe_{1-x} wetting layer of several angstroms in thickness on top of Si Ref.(5)

been mostly well reproduced and are shown in the tabular form in Fig.1.6 (from ref.(4)), where the magnetic order and the local moments, both experimental and numerical values, are reported. These compounds can show different magnetic orders such as ferromagnetic (FM), anti-ferromagnetic (AF), ferrimagnetic (FiM), non-collinear magnetic (NC), and nonmagnetic (NM). The authors have also mentioned about the nine phases whose magnetic order is either noncollinear or unknown, as well as the two configurations for which the simulations do not reproduce the experimental results. It is interesting to observe that some of the phases presented in ref.(4), such as Mn_5Ge_3, $Mn_{11}Ge_8$ and Mn_2Ge have already been found in the Mn-Ge system both as epitaxially grown over layers or segregated phases.

Well-defined Mn-rich nanocolumns whose composition is close to $MnGe_2$ have been recently grown(7). These columns where found to be embedded in a Mn-poor matrix, the overall system displaying a Curie temperature higher than 400 K. The formation of vertical one-dimensional nanostructures was observed for low growth temperatures (below 120°C(8)). The growth temperature and Mn content were found to affect the nanocolumn size and density. Actually, for temperatures higher than 180°C, the formation of

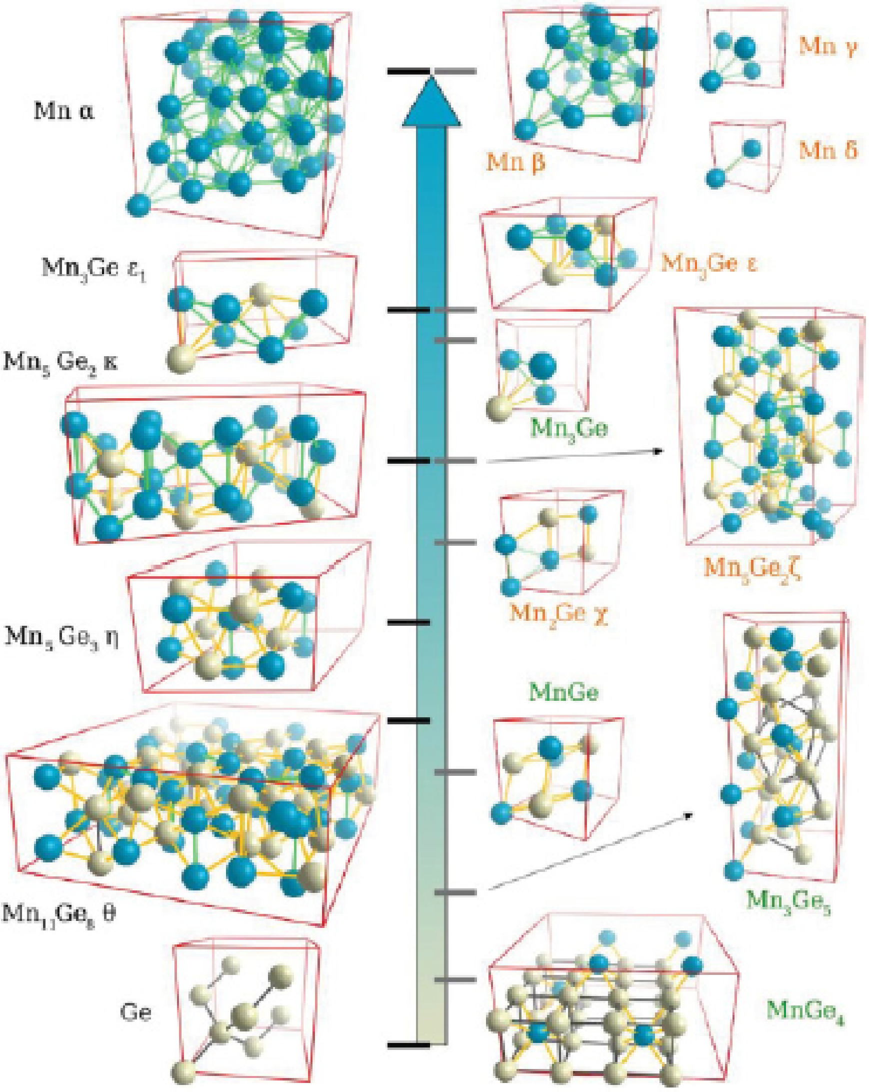

Figure 1.4: The known Ge-Mn compounds, ranging from 0 percentage Mn at the bottom to 100 percentage Mn at the top. Crystal lattices are shown, with, on the left-hand side, stable phases in the standard conditions of temperature and pressure (STP), and on the right-hand side, high-temperature (HT) compounds in orange and high-pressure (HP) compounds in green ref.(4).

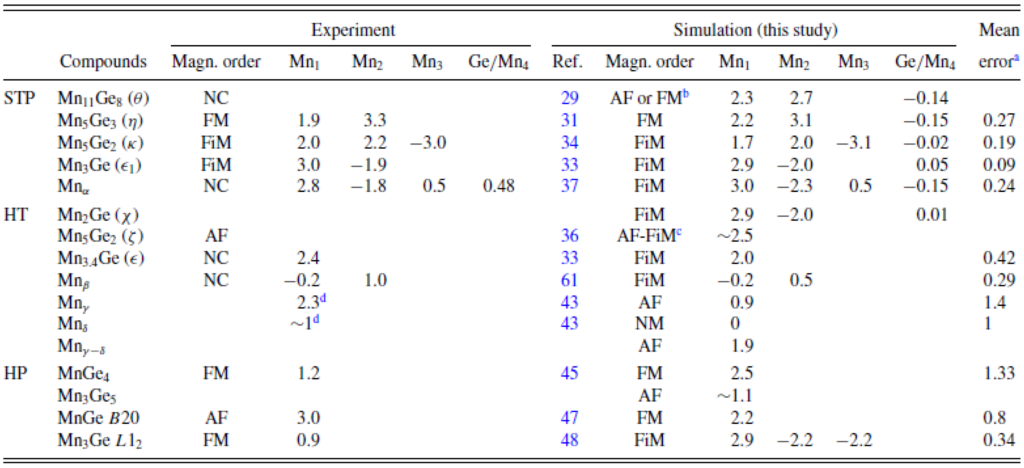

		Experiment					Simulation (this study)						Mean
	Compounds	Magn. order	Mn_1	Mn_2	Mn_3	Ge/Mn_4	Ref.	Magn. order	Mn_1	Mn_2	Mn_3	Ge/Mn_4	error[a]
STP	$Mn_{11}Ge_8$ (θ)	NC					29	AF or FM[b]	2.3	2.7		−0.14	
	Mn_5Ge_3 (η)	FM	1.9	3.3			31	FM	2.2	3.1		−0.15	0.27
	Mn_5Ge_2 (κ)	FiM	2.0	2.2	−3.0		34	FiM	1.7	2.0	−3.1	−0.02	0.19
	Mn_3Ge (ϵ_1)	FiM	3.0	−1.9			33	FiM	2.9	−2.0		0.05	0.09
	Mn_α	NC	2.8	−1.8	0.5	0.48	37	FiM	3.0	−2.3	0.5	−0.15	0.24
HT	Mn_2Ge (χ)							FiM	2.9	−2.0		0.01	
	Mn_5Ge_2 (ζ)	AF					36	AF-FiM[c]	~2.5				
	$Mn_{3.4}Ge$ (ϵ)	NC	2.4				33	FiM	2.0				0.42
	Mn_β	NC	−0.2	1.0			61	FiM	−0.2	0.5			0.29
	Mn_γ		2.3[d]				43	AF	0.9				1.4
	Mn_δ		~1[d]				43	NM	0				1
	$Mn_{\gamma-\delta}$							AF	1.9				
HP	$MnGe_4$	FM	1.2				45	FM	2.5				1.33
	Mn_3Ge_5							AF	~1.1				
	MnGe $B20$	AF	3.0				47	FM	2.2				0.8
	Mn_3Ge $L1_2$	FM	0.9				48	FiM	2.9	−2.2	−2.2		0.34

Figure 1.5: The different phases of the GeMn binary alloy, and their characteristics. Magnetic orders can be ferromagnetic (FM), anti-ferromagnetic (AF), ferrimagnetic (FiM), non-collinear magnetic (NC), and nonmagnetic (NM) (from ref.$^{(4)}$ and there in).

Mn_5Ge_3 clusters is evidenced, while for intermediate growth temperatures nanocolumns and nanoclusters coexist.

System with $Mn_{11}Ge_8$ ferromagnetic clusters embedded in a Mn_xGe_{1-x} dilute ferromagnetic semiconductor matrix have also been found$^{(14)}$. Clusters were shown to dominate the magnetic properties and exhibited a ferromagnetic ordering temperature of approximately 300 K, while the matrix was found to play a subtle but interesting role in determining the transport properties .

Recently, the possibility of growing precipitate-free Mn-doped Ge system have been reported$^{(15)}$, with doping levels near the kinetic solubility limit and a growth temperature of 95^{o}C. These samples show interesting contrasts and similarities of magnetic properties with those of heavily doped DMS, indicating that the substitutional Mn contents are very similar, offering useful opportunities for studying the fundamentals of carrier-mediated exchange and metal-insulator transitions without complications arising from precipitate formation.

The search for high Curie temperature ferromagnets in the Mn-Ge system was not only focussed on bulk-like DMS, but was also extended to the domain of surface science. The main goal is the search for ferromagnetic epitaxial metal/semiconductor interfaces with good potential for spin injection in a

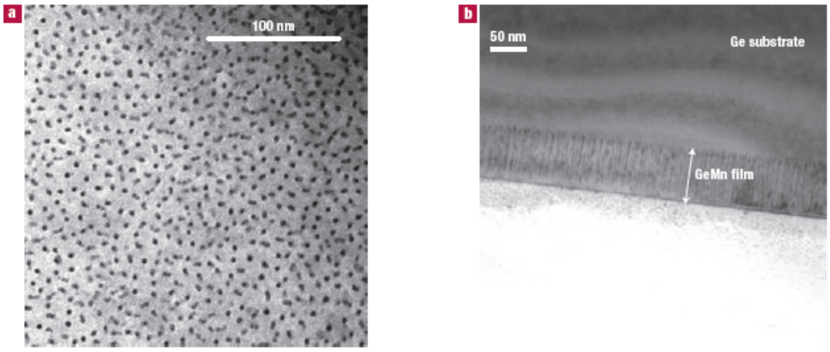

Figure 1.6: Transmission electron micrographs of an 80-nm-thick $Ge_{0.94}Mn_{0.06}$ film. a, Low-magnitude plane view, the dark spots are nanocolumns. b, Low-magnitude cross-sectional image of the 80-nm-thick (Ge,Mn) layer, the nanocolumns are perpendicular to the film plane and appear as dark lines from ref.(7).

silicon-compatible geometry.

Subsurfactant epitaxy was established as a conceptually new approach for introducing manganese as a magnetic dopant into germanium substrate(16). A kinetic pathway was devised in which the subsurface interstitial sites on Ge(100) are first selectively populated with Mn, while lateral diffusion and clustering on or underneath the surface are effectively suppressed. Doping levels at the order 0.25 at. percentage of Mn has been able to give rise low temperature ferromagnetic ordering, but the Curie temperature exceeds room temperature by a comfortable margin. In the Fig. 1.7, STM images are shown for 0.05 ML of Mn on Ge(100) deposited at 150 K (a) and RT (b), respectively.

Ferromagnetic Mn_5Ge_3 thin films grown on Ge(111) with solid-phase epitaxy have also been reported(10,12). The alloy films exhibit metallic conductivity and strong ferromagnetism up to the Curie temperature, T_C 296 K. It is shown that $(\sqrt{3} \times \sqrt{3})R30^\circ$ surface reconstruction of the Mn:Ge(111) interface can be considered as the seed structure for growing ferromagnetic epitaxial layers. Deposition of approximately one monolayer of Mn and subsequent annealing has been resulted in the formation of Mn_5Ge_3 islands(11). For an intermediate regime (4 to 190 ML), the Mn:Ge(111) surface was always found metallic, displaying a structural ordering identified by the surface $(\sqrt{3}\times\sqrt{3})R30^\circ$ reconstruction(12). Figure 1.8 shows the typical scanning tun-

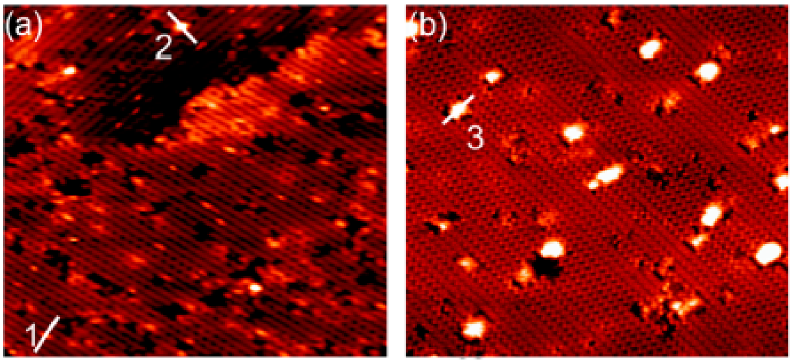

Figure 1.7: STM images of 0.05 ML Mn on Ge(100) deposited at 150 K (a) and RT (b), respectively from ref. (16).

neling microscope (STM) image with a honeycomb structure consistent with the $(\sqrt{3} \times \sqrt{3})R30^\circ$ surface reconstruction.

In the present thesis, we will compare the electronic properties of an ordered metallic Mn:Ge(111) thin interface (related with the Mn_5Ge_3 phase) with those of a Mn_xGe_{1-x} diluted alloy, that can be regarded as a diluted magnetic semiconductor DMS. Our attention is focused on the DMS, as core level photoemission data on this kind of system are virtually missing, in spite of a large set of X-ray absorption data collected at the Mn L-edge. In addition to this, electron dynamics has been investigated through an analysis of resonant photoemission measurements (Chapter 3), in the case of an ordered metallic Mn:Ge(111) interface. In many respects, the two compounds represent the end-points of the Mn-Ge system: while the former is ferromagnetic and metallic, the latter is semiconducting and, in the present case, weakly paramagnetic due to the low amount of Mn ions diluted in the sample.

1.3 Mn-doped III-VI semiconductors as possible DMS

The III-VI semiconductors GaSe, InSe, GaTe, and GaS have received considerable interest in the last few years because they show remarkable nonlinear optical properties and they are regarded as promising materials for photo-electronic applications. Furthermore, the magnetic properties of these systems doped with transition metal ions (e.g. Mn or Fe) are currently

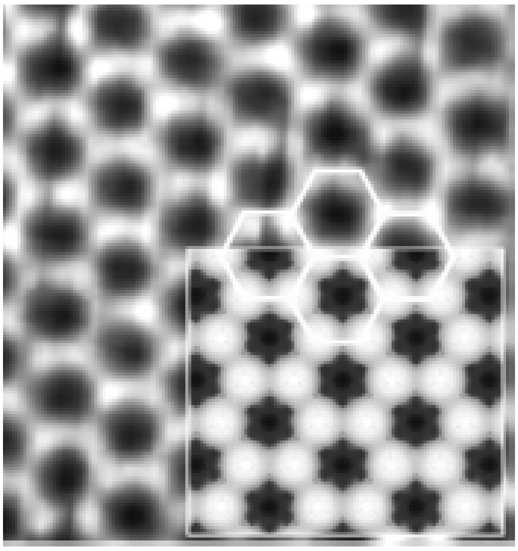

Figure 1.8: Filled-state STM images from the surface of a Mn5Ge3 thin film: 5.3 nm x 4.5 nm. The inset is the simulated filled-state image from DFT ref.$^{(10)}$.

under investigation with the aim to find out new classes of diluted magnetic semiconductors.

Among these compounds, a new class of III-VI diluted magnetic semiconductors (III-VI DMS) has been identified, which includes systems of the form $\mathrm{A}^{III}_{1-x}\mathrm{M}_x\mathrm{B}^{VI}$, where $\mathrm{A}^{III}\mathrm{B}^{VI}$ is a III-VI semiconductor and M is a transition metal ion. For instance, Mn has been incorporated into $GaSe(0001)$ in samples grown from the melt, and intriguing magnetic properties have been found$^{(81)}$. A short range anti-ferromagnetic ordering has been invoked to explain the rather complex magnetic behavior, but a clear identification of the short range coupling mechanisms related to these experimental evidences is still missing. Moreover, a clear understanding of the interplay between magnetism and electronic properties has not yet been reported so far, mainly due to the difficulty of growing high quality Mn-doped single crystals and control both the doping level and possible phase segregations or the creation of defects and vacancies upon doping. Finally, the local structure around Mn atoms at the Mn:GaSe interface has not yet been probed, being the mechanism of Mn diffusion in the lattice poorly investigated. This is important in order to relate the observed magnetic behavior to either direct or superexchange interactions through $Mn-Mn$ or $Mn-Se-Mn$ bonds,

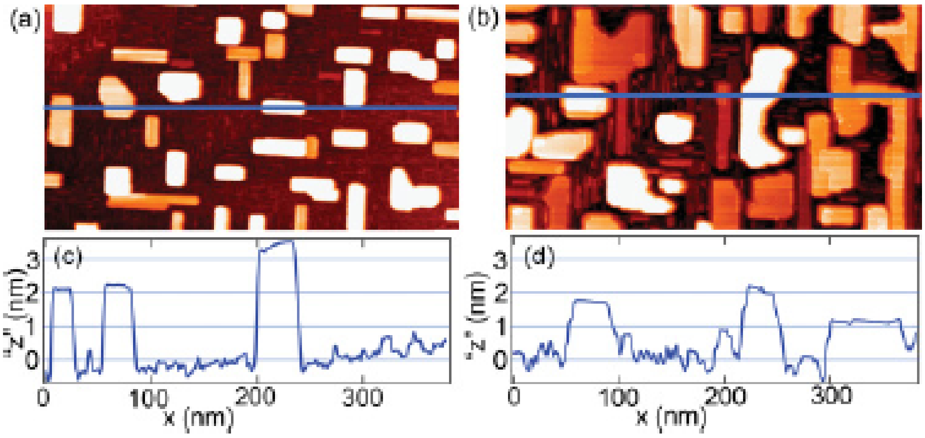

Figure 1.9: STM images comparing island morphology for buffer (a) D8 and direct (b) B4 films with similar QCM (quartz crystal monitor) thickness (~3 nm) and QCM Mn concentration (~8 %), ref.(82).(c) and (d) are line profiles through (a) and (b), respectively.

respectively.

Incidentally, a recent paper(82) on the Mn:Ga_2Se_3 system has drawn the attention on the magnetic behavior in this interface, that is strictly related to the case of Mn-doped on ϵ-type GaSe(0001) under consideration in the present thesis. In the study of Lovejoy *et al.*, the growth and phase segregation properties of the potential dilute magnetic semiconductor alloy $(MnSe)_x(Ga_{2/3}Se)_{1-x}$ are studied as a function of thickness, Mn concentration, postgrowth annealing, and the presence or absence of undoped Ga_2Se_3 buffer and capping layers. STM images comparing island morphology for buffer and direct films with similar thickness (~3 nm) and Mn concentration (~8 percentage) are shown in Fig.1.9. Instead of only one kind of phase, many possible phases like $MnGa_2Se_4$, MnSe, $(MnSe)_x(Ga_{2/3}Se)_{1-x}$ have been speculated to be present on the surface/interface.

A schematic diagram of epitaxial relationship between Ga_2Se_3 film and MnSe islands along [110] and three-dimensional perspective view have been shown in the Fig. 1.10 (from ref.(82)).

As in the case of the Mn-Ge system, phase segregation is a relevant problem to be addressed in the search of intrinsic magnetism in III-VI compounds. For this reason, one has to consider all possible phases in the Mn-Ga-Se

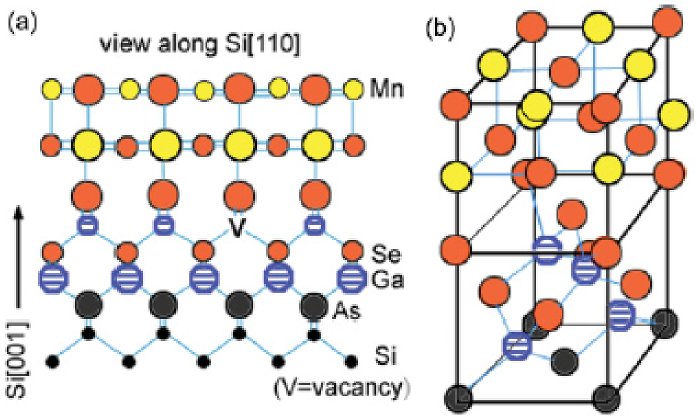

Figure 1.10: A Schematic diagram showing epitaxial relationship between Ga_2Se_3 film and MnSe islands along [110] (a) and in three-dimensional perspective view (b). The whole interface was grown onto a Si (001) surface with an As buffer layer. The rocksalt MnSe and defected zinc-blende Ga_2Se_3 over Si(001) are aligned such that the Se fcc sublattice continues across the interface (ref.(82) and Refs. therein).

system, either binary or ternary. So far we know that neither MnSe nor $MnGa_2Se_4$ exhibits ferromagnetism. $MnGa_2Se_4$ is antiferromagnetic with a Néel temperature of 8 K.(89). MnSe case is more complicated, as structural transitions occur simultaneously with magnetic transitions to antiferromagnetism between 90 and 300 K(90). The magnetism in the single crystal of Mn-doped layered GaSe(81) exhibits an unusual temperature dependence, where the magnetization increases with increasing temperature between 100 and 170 K. A re-entrant carrier-mediated ferromagnetic semiconductor is proposed to explain its magnetic behavior.

Like the II-VI DMS, substitutional magnetic ions in the III-VI DMS are in a (distorted) tetrahedral environment. However, in sharp contrast to the II-VI DMS, the III-VI semiconducting host presents a two dimensional (2D) nature. The weak van der Waals bonding between the stacked four atom thick layers further enhances the two-dimensional nature of this crystal. Because of it's markedly nearly 2D structure, GaSe has been considered in the past for angle-resolved photoemission (ARPES) experiments, and a recent study has refocused the interest on this aspect by providing new ARPES data(83). To the best of our knowledge, there is a little understanding about the electronic structure of Mn-doped GaSe. Furthermore, GaSe is an ideal system for surface studies. It cleaves well and Mn diffusion through the surface can be triggered by different annealing temperatures, yielding a potential rich phase diagram, with interesting magnetic properties at the surface/interface.

1.4 Thesis Outline

In **Chapter 2**, the experimental and computational details on X-ray spectroscopy of interest are presented. The physical principles and the experimental setups underlying the X-ray photoemission (XPS), X-ray absorption (XAS) and the resonant photoelemission (ResPES) spectroscopies are described; a brief introduction to parameterized, configuration integration (CI), models is described, as this approach has been adopted to calculate the Mn spectral weight in core-level and valence band photoemission.

In **Chapter 3**, the electronic and magnetic properties of the Mn-doped on Ge(111) surface/interface are described. Preparation of Mn:Ge surface-/interface, which is a Mn_xGe_{1-x} diluted magnetic semiconductor (DMS) system, as evidenced by Mn 2p line shape from the XPS has been explained. A parameterized CI model is used to calculate the experimental spectrum. The information on the electronic interaction between the localized Mn ions and the ligand orbitals in the system is described(92). The magnetic behavior of these systems has been explored by SQUID magnetometry measurements.

In **Chapter 4**, we have prepared an ordered metallic Mn_5Ge_3 ultra-thin interface. The electronic properties of the sample have been studied by XPS, XAS, and ResPES techniques. In particular, the ResPES technique has been a very useful tool to investigate the dynamics of valence electrons triggered by the Mn 2p-3d transition(91). The physical basis of ResPES have been presented in Chapter 2.

In **Chapter 5**, the Mn-doped ϵ-GaSe(0001) surface has been explored starting from growth and characterization. Evaporation of Mn for 9 consecutive steps on an ultra high vacuum cleaved ϵ-GaSe(0001) surface has been done. XPS results shows that Mn substitutes Ga site at the surface, for low Mn concentrations. In this case we were interested to explore the cation substitution mechanism, along with the limits of Mn dilution before the onset of Mn segregation processes at the surface. Once the segregation limits have been established, we prepared a new sample, with a Mn content below this limit in order to study the electronic, and magnetic, properties the

$Ga_{1-x}Mn_xSe$ surface alloy obtained by thermally-driven diffusion of Mn ions evaporated on the surface of a freshly cleaved ϵ-GaSe(0001) single crystal. The surface electronic properties of this system have been explored by core and valence band photoelectron spectroscopy, XAS, and ResPES. Parameterized CI models have been used to calculated Mn spectral weight in core and valence band photoemission(93).

1.5 Publications

Here is the list of the articles already published (†) or in preparation (‡) related to this Thesis work:

1. † L. Sangaletti, S. Dash, A. Verdini , L. Floreano, A. Goldoni, G. Drera, S. Pagliara, A. Morgante; *Tracking the excitation dynamics in the Mn:Ge(111) metallic interface by resonant electron spectroscopy*, *J. Phys.: Condens. Matter.* **24** 24 (2012) 235502

2. † S Dash, M C Mozzati, P Galinetto, G Drera, S Pagliara and L Sangaletti; *Electronic properties and magnetism of Mn:Ge(111) interfaces probed by core level photoemission spectroscopy*, accepted *Journal of Physics: Conference Series, SCES-2011, Cambridge, UK*

3. ‡ S. Dash, M C Mozzati, G. Drera, P Galinetto, F. Bondino, E. Magnano, V. Aguekian, L. Sangaletti; *Search of novel electronic and magnetic properties at Mn:GaSe(0001) interface*, in preparation.

4. ‡ S. Dash, G. Drera, P Galinetto, M C Mozzati, V. Aguekian, L. Sangaletti ; *Mn diffusion at the Mn:GaSe interface: a quantitative analysis based on X-ray Photoemission data*, in preparation.

1.6 Acknowledgements

The author wishes to acknowledge all the people involved in this thesis work:

- Maria Cristina Mozzati, Pietro Galinetto of the Universitá di Pavia for their (enormous) work on the Squid magnetometry measurement of Mn:Ge and Mn:GaSe samples.

- V. Aguekian of the V. A. Fock Institute of Physics, St. Petersburg State University, 198504 St. Petersburg, Russia for providing GaSe Single crystals.
- Federica Bondino, Elena Magnano and the staff of the BACH beamline at the ELETTRA synchrotron (Basovizza, Trieste),Italy
- Aleberto Verdini, Luca Floreano and Alberto Morgante and the staff of the ALOISA beamline at the ELETTRA synchrotron.
- Luca Petaccia and the staff of the BaDELPh beamline at the ELETTRA synchrotron.
- Emanuele Cavaliere, Nanoscience Lab. of the Universitá Cattolica di Brescia, Italy for using Atomic Force Microscope (AFM).
- Luigi Sangaletti, Giovanni Drera, Patrizia Borghetti, Federica Rigoni and Gabriele Salvinelli of the Surface Science and Spectroscopy Lab. of the Universitá Cattolica di Brescia, Italy.

Chapter 2

Experimental Techniques and Parameterized CI Calculations

2.1 Introduction

The experimental methods applied in this thesis work are X-ray photoemission spectroscopy(XPS), x-ray absorption (XAS), angle resolved photoemission (ARPES) and photoemission taken at resonance condition (ResPES) and magnetic characterization (SQUID). In both Mn-doped Ge(111) and GaSe interfaces, magnetic characterization has been done with SQUID magnetometery at University of Pavia. X-ray photoemission measurements have been carried out in the Surface Science and Spectroscopy Lab at Universita Cattolica del Sacro Cuore, Brescia and while X-ray absorption, resonant photoemission and angle resolved photoemission data have been collected at BACH, ALOISA and BaDElPh beam lines at the Elettra synchrotron light source in Trieste (Italy). A relevant part of this thesis work has been carried out by soft X-ray spectroscopic techniques. The main advantage of using X-rays is the possibility to be chemically selective and thus to have access to electronic structure of a single ionic species. Mn core level and valence band photoemission spectra have also been calculated by a parameterized CI model. In the following, x-ray experimental techniques and theoretical models will be described.

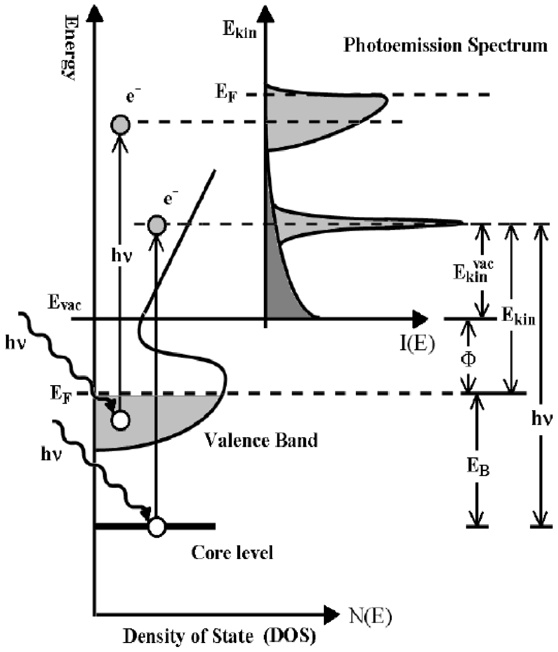

Figure 2.1: Schematic view of X-ray photoemission spectroscopy.

2.2 X-ray Photoelectron Spectroscopy

X-ray photoemission spectroscopy is a well established photon-in electron-out technique that gives access to the electronic and chemical properties of selected atomic species on a sample surface.

A schematic view of XPS is shown in Fig. 2.1. In an XPS experiment the specimen is exposed to a soft X-ray source (usually $h\nu \geq 100$ eV) in order to induce the photoelectric emission from core-levels and valence band. The number of electrons vs the kinetic energy (E_k) spectrum is measured by an electron spectrometer.

The survey spectra are usually composed by a series of peaks superimposed to a stair-like structure (see for example, the Mn-doped Ge(111) survey in Fig. 2.2); the peak energy is related to a specific core level of an atom or to secondary Auger electrons induced by the core-hole, while the step-like background is generated by the inelastic scattering of photoelectrons. XPS peaks ascribed to a core-level with a symmetry different than spherical s, can be split by spin-orbit interaction, which is inversely proportional to n quantum

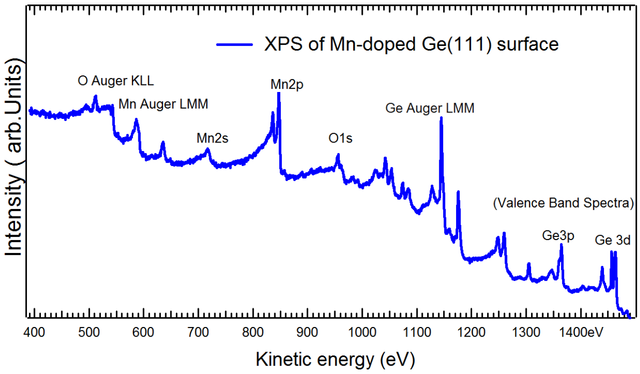

Figure 2.2: XPS survey spectrum of Mn doped Ge(111) surface taken with photon energy of Al k_α source.

number. The relativistic intensity of the spin orbit split components scales as 2j+1. For example the p levels are split in $p_{1/2}$ and $p_{3/2}$ components, with area ratio 2:4 and so on).

Since the core-level energies are mostly determined by the atomic species, XPS allows the identification of the sample composition (chemical elements and their relative ratio); moreover, the specific valence state of the atom affects the position of the core-level peaks energies, allowing the identification also of the bond ionicity (or covalency) degree. This is the reason why XPS is also known as ESCA, Electron Spectroscopy for Chemical Analysis.

2.2.1 Experimental Set-Up

A standard XPS set-up requires an experimental chamber operated in UHV conditions (10^{-10} mbar) in order to avoid sample contamination and, to lesser extent, to avoid the photoelectrons scattering through the analyzer. The commercial X-Ray sources are usually based on the emission spectra of aluminum (Al k_α line, $h\nu = 1486.7$ eV) and magnesium (Mg k_α, $h\nu = 1256.6$ eV), but of course XPS can be performed with the synchrotron radiation in dedicated beamlines, in order to have tunable photon energies and a higher photon flux.

In the Universitá Cattolica Labs a dual anode (Mg/Al) PSP X-ray source with a Scienta R-3000 AR-XPS analyzer with a 2D phosphor detector have been used. The best resolution was 0.7±0.1 eV, mainly due to the X-ray source. This analyzer can operate both in a “transmission” mode and in an "angular mode" that allows the simultaneous collection of the XPS spectra in a ±10° range. When an higher resolution was needed, a parallel XPS setup has been used with a monochromatized Al k_α source and a VG MkII system, leading to a 0.5 eV total resolution at the expense of the total electron count rate.

2.2.2 XPS Theory

From the conservation of total energy, the kinetic energy of an electron photoemitted from a core-level can be expressed as follows:

$$E_{Kin} = h\nu - E_{Bin} - \Phi \tag{2.1}$$

where E_{Bin} is the electron binding energy and Φ is the work function, which is the extra energy needed to transport an electron from the sample to the analyzer. The electrons from Auger process are related only to internal atomic relaxation and thus are photon-energy independent (i.e. fixed kinetic energy), while the kinetic energy of core-level photoelectrons changes with the photon (fixed binding energy). A tunable (multiple anode, or synchrotron based) X-ray source can thus be used to better identify Auger structures, when superimposed to other core-levels.

The probing depth of this technique is due not to X-ray penetration (in the μm range) but to the inelastic mean free path (IMFP) of electrons in solids which, at these kinetic energies, is in the order of 1-2 nm: XPS is thus a surface-sensitive technique. In some synchrotron facilities, the photoemission with hard X-ray photons (HAX-PES, $h\nu$ up to 10 keV) is also possible, which in turn is a bulk-sensitive technique; in HAXPES however one has to deal with respect to the conventional x-ray, with smaller photoelectron cross-sections.

From a quantum-mechanics point of view, the photoemission process can be written as follows with the Fermi Golden rule:

$$W_{ph} = \frac{2\pi}{\hbar} \left|\langle i|T|f\rangle\right|^2 \delta(E_k + E_i - E_f - h\nu) \tag{2.2}$$

where the squared matrix element gives the transition rate and the Dirac delta accounts for energy conservation; in photoemission, the final state is the ground state plus a core hole and a free (photo emitted) electron with

E_k energy. The matrix operator T for the electron-photon interaction can be taken as the simple dipole operator $T = e \cdot \vec{r}$, since the contribution of the quadrupole operator for the soft X-ray regime is negligible$^{(66)}$. This equation can be solved with the Green functions method, in order to account for scattering process and final state effects due to the relaxation of the electronic levels in the proximity of the core-hole; this approach is called the "one-step" photoemission theory.

Another way to describe XPS is the so-called "three-step" model, in which the process is described in three different steps:

- the first step is the photoemission from the atom, described with photoemission cross section;
- the second step is the drift of the electron in the solid, described by the electronic IMFP;
- the third step is the escape of the photoelectron from the solid, described by the work-function.

The three-step model is often assumed in the framework of the *sudden approximation*, in which one supposes that the core-hole final state does not influence the XPS spectra, while the one-step model gives a good description of excitonic effects and plasmon resonances.

In the three-step model, the intensity (i.e. the area) of a photoelectron peak depends on many parameters; disregarding the diffractive effects and X-ray attenuation (important only for grazing photon incidence angles), the contribution to the photoemission intensity of an infinitesimal thick layer at depth z from the surface can be expressed as follows:

$$dI = \phi D_0(E_K)\sigma(h\nu)\rho A_0 P(\lambda, z, \theta) dz \tag{2.3}$$

where

$$P(\lambda, z, \theta) = e^{-\frac{z}{\lambda cos(\theta)}} \tag{2.4}$$

and:

- ϕ is the photon flux;

- D_0 is the analyzer transmission function that depends on the kinetic energy;

- σ is the photoelectron cross section that depends on the atomic species, the electronic level (i.e. 1s,2s,2p...) and the photon energy;

- ρA_0 is the number of atoms per unit volume per sampling area, that can depend on the X-ray focalization on the sample and/or on the analyzer focus;

- $P(\lambda, z, \theta)$ is the probability of an electron at depth z to escape from the specimen and to reach the analyzer placed at an angle θ relative to the sample normal; λ is the IMFP and depends on the sample composition and on E_k.

When dealing with the elements ratios only, the photon flux and sampling area can be discarded since they are contributing in the same way to each photoelectron peak. When measuring XPS peaks with close kinetic energy (or with a well calibrated analyzer) also the D_0 term can be neglected. The other parameters have to be taken into account to carefully quantify the elements concentration; the typical accuracy of this method in a homogeneous sample is around 1-5%. The typical XPS sensitivity is about 0.1-1%.

The parameter P in Eq. 2.4 is also dependent on orientation of specimen with respect to the analyzer; in fact, at grazing emission, photoelectrons of inner layer have to travel for a longer path through the sample in order to reach the vacuum, resulting in a reduced photoelectron intensity from the bulk. The surface sensitivity of XPS is thus improved at grazing emission angles; this can be useful for instance for enhancing the contribution of absorbed molecule respect to the host substrate.

This effect can be also used in a reverse way: for example, in the case of a thin film coverage of a bulk material, one can use AR-XPS data to estimate the overlayer thickness. This is only possible when the composition of each layer is known, in order to fix all the parameter described in Eq. 2.3; in some cases just a single measure (i.e. taken at only one emission angle) could be sufficient to estimate thickness, but of course a set of data taken at different angles can improve the results reliability.

2.3 X-ray Absorption Spectroscopy

In a XAS experiment, the X-ray total absorption cross-section of the specimen is measured. Therefore, XAS requires the possibility to scan the photon energy and thus it is usually performed on synchrotron facilities, even if similar spectra can be obtained through the electron energy loss spectroscopy (EELS) which formally share the same theoretical formalism. While XAS is the most generic name, many different notation are given according to the required experimental information or to the specific application fields; here is a list of the different XAS definitions:

- NEXAFS (Near-Edge X-ray Absorption Fine Structure) or XANES (X-ray Absorption Near-Edge Structure): in both cases the absorption cross section is measured "near" the absorption edges of a specific elements. Although from an experimental point of view are both similar, in general NEXAFS is used in surface or molecular studies and XANES in crystal or bulk studies. The NEXAFS experimental information covers the empty states, the adsorbate geometry (NEXAFS) and the symmetry of a specific atomic species (XANES).

- EXAFS (Extended X-ray Absorption Fine Structure): in this case, the absorption cross section is collected over a wider energy range. In ordered structures, these spectra show oscillations due to multiple scattering of excited electrons: by analyzing the Fourier transform of the EXAFS spectra it is possible to evaluate the nearest-neighbors bond lengths.

- SEXAFS (Surface Extended X-ray Absorption Fine Structure): same as EXAFS, but tuned to give more information on the surface bond lengths.

- XMCD and XLD (X-ray Magnetic Circular Dichroism and X-ray Linear Dichroism): XAS spectra taken with different X-ray polarization. XMCD requires a magnetic field (both of specimen or external) and gives direct information on the local magnetism; XLD can give further information on the symmetry distortion of the ionic environment. These techniques can be done also in an imaging-like fashion, both scanning the sample position or using electronic lenses, giving the possibility to map the magnetic or structural domains of the specimen.

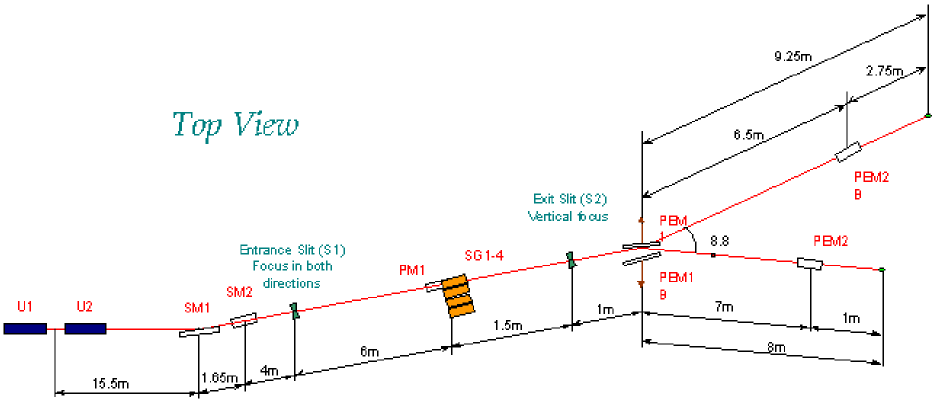

Figure 2.3: Top view of BACH beamline layout at ELETTRA synchrotron. From left to right are depicted the undulators (U_1 and U_2) on the storage rings, then the mirrors, the slits, the monochromator and the user end-stations.

In this thesis XANES measurement are reported. Further details about experimental set-up and theory will be given in the next paragraphs.

2.3.1 Experimental Set-Up

Most of XAS data on Mn:GaSe and Mn:Ge shown on this thesis have been collected on BACH and ALOISA beamlines at the ELETTRA synchrotron in Trieste (Italy). A synchrotron X-ray source combines an high brilliance, a small on-target X-ray focus as well as the photon-energy and polarization tunability.

In Fig. 2.3, a schematic view of the BACH (Beamline for Advanced diCHroism) beamline set-up has been shown. The photon energy is tuned by changing the distance (usually referred as "gap") of undulators magnets and by means of a two mirror monochromator. The resolving power ($\Delta E/E$) at BACH beamline is 20000-6000, 20000-6000, and 15000-5000 in the energy ranges 40-200 eV, 200-500 eV, and 500-1600 eV, respectively.

A detailed ResPES study of the Mn:Ge(111)interface(91) is presented in chapter 4. The experiment has been carried out on the ALOISA beamline, elettra, Italy which is a multipurpose beamline, which offers a wide range of complementary experimental techniques like photoemission spectroscopy, photoelectron diffraction, X-ray diffraction etc. A peculiar monochromator has been developed which covers a very wide energy range from 120 eV to

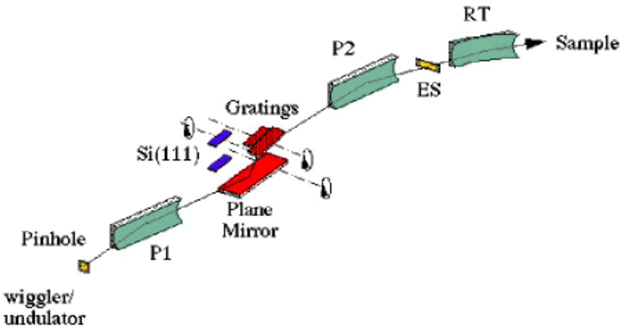

Figure 2.4: ALOISA beamline at ELETTRA synchrotron as shown above.

8000 eV. The resolving power at ALOISA beamline is 4000-8000, 2000-4000 and 7500in the energy ranges 120 - 1000 eV, 1000 - 2000 eV and 3000 - 8000 eV respectively.

A schematic view of the ALOISA (Advanced Line for Overlayer, Interface and Surface Analysis) beamline setup is given in figure 2.4.

As in XPS, XAS requires UHV conditions and, because of synchrotron high photon-flux, can suffer of charging effects. The X-ray polarization can be tuned with dedicated insertion devices (helical undulators) or by exploiting the natural polarization characteristic of synchrotron light.

The absorption cross section could be in principle detected by measuring the photon flux before and after the sample; in practice, this method can be applied only to very thin (in the range on μm) samples. Usually XAS is performed by measuring secondary de-excitation process caused by the absorption of X-rays. Here is a summary of detection technique:

- Fluorescence: XAS can be measured by detecting the rate of fluorescence given by the recombination of the electrons with the core-hole created by the excitation. This detection technique requires the presence of a silicon-based photon detector in the measurement chamber and its sensitivity is related to the X-rays penetration depth in the sample (in the μm range). Fluorescence detection is less effective in light materials, since the Auger decay is the most probable de-excitation process, and can be quenched in very dense material, because of the re-absorption of the emitted photon. However, It doesn't suffer of charging effects, even in insulating samples.

- Total yeld: XAS can be detected by measuring the electrical current ("drain current") generated by the X-ray absorption. A picoammeter is needed, since this current ranges typically on the 10^{-10}- 10^{-7} A scale. The drain current is generated by a cascade of Auger process that are also related to the electrons inelastic scattering. Since only the electrons that reach the surface contribute to this current, the probing depth is lower than in fluorescence detection.

- Partial yeld: the photoemission intensity is usually proportional to the absorption cross section, thus XAS can be measured by integrating the photoelectron emission in a defined energy range, through a channeltron detector or an electron analyzer. This detection technique is the most surface-sensitive and, like XPS, can be affected by charging effects in insulating samples.

Spectra should be normalized with the incoming photon flux, which is usually measured on the monochromator last mirror through the drain current method.

2.3.2 XAS Theory

A schematic view of XAS is shown in Fig. 2.5. In short, when the photon energy is higher than a core-level binding energy, an electron from that core level could be excited into an empty states below the Fermi edge. The transition rate for this process can be described with Fermi Golden rule, similarly to Eq. 2.2:

$$W_{ph} = \frac{2\pi}{\hbar} \left|\langle i|T|f\rangle\right|^2 \rho(E_f - E_i - h\nu) \tag{2.5}$$

where ρ is the empty level density of states (DOS). As in XPS, the operator T can be taken as the usual dipole operator $e \cdot \vec{r}$. In the case of most core-level edges, except in transition metals and rare earths, with photon energy between 100-2000 eV the dipole operator is slowly varying with $h\nu$; in this case, the XAS spectra becomes a direct measurement of the empty DOS, plus a contribution from electrons multiple scattering(67).

In the case of open-shell system, such as transition-metals (TM) or rare-earths (RE), the electrons excited in the empty states can strongly interact together and with the core-hole. In such system, the matrix element of

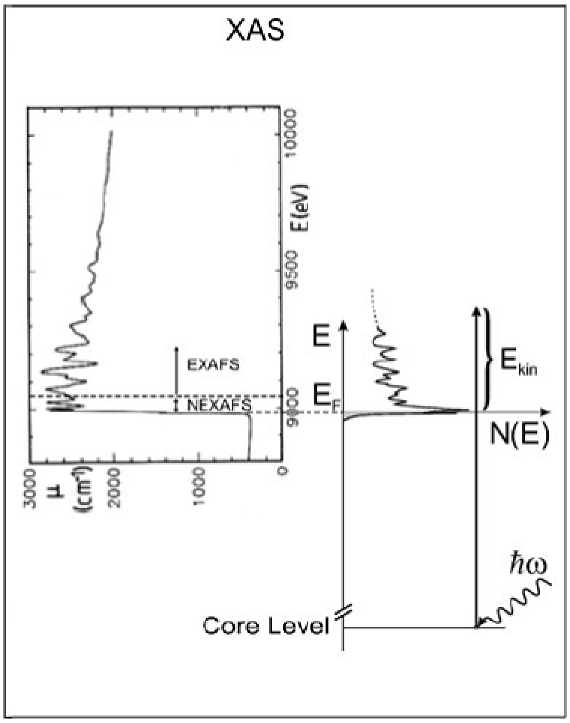

Figure 2.5: Schematic view of X-ray absorption spectroscopy

Eq. 2.5 becomes the leading term and multiplet features appears in the spectrum. Since many experimental data of this Thesis have been taken at the Manganese 2p threshold, the multiplet effects are explained in more details in the Section 2.6.

2.4 Resonant Photoelectron Spectroscopy

Resonant Photoelectron Spectroscopy is a powerful technique to measure the valence band (VB) X-ray photoemission where the photon energy is tuned across the specific atomic x-ray absorption edge. Below the absorption edge, the direct photoemission from the occupied electronic states only contributes to the VB photoemission spectra, whereas at the X-ray absorption edge the spectra display contributions of two emission channels namely direct photoemission and auto ionization that are simultaneously present and can interfere with each other(41,75).

In a single-particle approach (i.e. multiplet calculations and related approximations) the direct valence band photoemission channel ($c^m v^n \rightarrow c^m v^{n-1} + e^-$) can interfere with the autoionization channel caused by the presence of a core-hole ($c^{m-1} v^{n+1} \rightarrow c^m 3d^{n-1} + e^-$). As a result, the part of the valence band related to the specific atomic species can be greatly enhanced (or suppressed). This effect is known to occur for most of the elements, both organic and inorganic. Following the description of Brühwiler et al.(75), a pictorial representation of the process is given in Fig. 2.6. In this figure the most important excitation and de-excitation processes related to the ResPES technique are shown.

On the left part the photoemission-related channels are shown: Fig. 2.6(a) shows the normal valence band photoemission (VPES) and Fig. 2.6(b) the core-level photoemission. In the latter case, the system can fill the core-hole through a normal Auger decay (Fig. 2.6(c)) or through fluorescence, which is not usually measured during a conventional ResPES experiment. In Fig. 2.6(d) the resonant transition from the core level to the empty state is depicted (i.e. X-ray absorption). In this case the system can relax by filling the core-hole with a valence band electron, opening two different autoionization channels: Fig. 2.6(e) shows the emission of the excited electron from the empty states, labeled as *participant decay* and Fig. 2.6(f) shows the emission of another electron from the valence band, labeled *spectator decay.* The final state of the participant decay is equivalent to the valence band photoemission

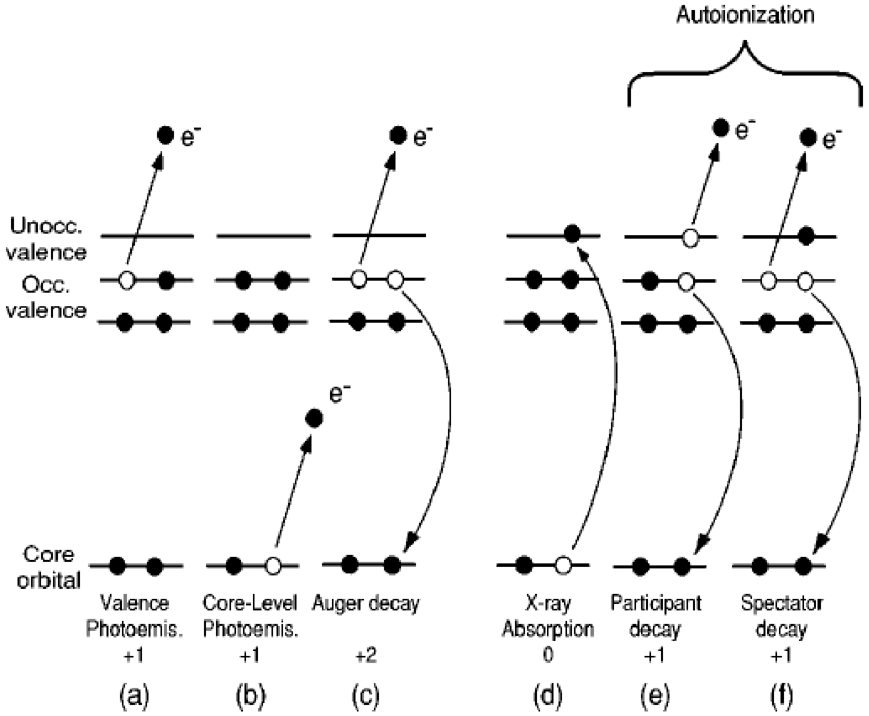

Figure 2.6: Schematic of the possible excitation and de-excitation channels in a ResPES experiment.

one, leading to the (constructive or destructive) interference effect. While tracking the electronic excitation across an X-ray absorption threshold, a set of different channels can be explored, namely normal photoemission spectroscopy (PES), resonant photoemission spectroscopy (ResPES), resonant Auger emission (RAE), resonant Raman Auger spectroscopy (RRAS) and normal Auger emission (the two-hole valence band satellite of Ref.(42,45)). Below the absorption threshold, the normal photoemission channel from valence levels is active, as the photon energy is not high enough to create a core hole. As one approaches the absorption threshold, the autoionization channel is enabled. If the excited electron participates in the decay process (participator decay), the outgoing electron receives an energy equal to the photon energy and this autoionization channel can interfere with the direct photoemission channel to yield the so-called ResPES. If the excited electron does not participate in the decay process (spectator decay) and remains in the excited level during the core hole decay, the autoionization channel becomes more similar to an Auger emission, but the excited electron still remains in an energy level low enough to screen the core attraction, thereby increasing the kinetic energy of the secondary electron. Therefore the RAE emission (corresponding to a two-hole one-electron final state) appears at KE slightly higher than in the normal Auger case. For higher photon energies the systems turns out to show a normal Auger emission, along with a normal photoemission. In this regime, the excited electron has no relevant interaction with the core hole, and cannot affect the de-excitation dynamics which turns into a normal Auger, two-hole, final state. Alternatively, the RRAS to normal Auger transition can be thought to occur when the electron excited in the intermediate state delocalizes faster than the lifetime of the initial core hole.

In fact, in an highly delocalized (metallic) band the extra electron can be quickly removed, quenching the ResPES channel to the normal Auger. ResPES is thus a useful experimental tool to evaluate the charge-transfer process, especially between a substrate and deposited molecules or atoms. When applied for this purpose, the ResPES technique is usually referred to as Core-Hole-Clock (CHC) spectroscopy. The interference intensity can be calculated in the Fermi golden rule approach as follows(78):

$$\omega = 2\pi \sum_f \left| \langle f|V_r|g\rangle + \sum_m \frac{\langle f|V_A|m\rangle\langle m|V_r|g\rangle}{E_g - E_m - i\Gamma_m/2} \right|^2 \delta(E_f - E_g) \tag{2.6}$$

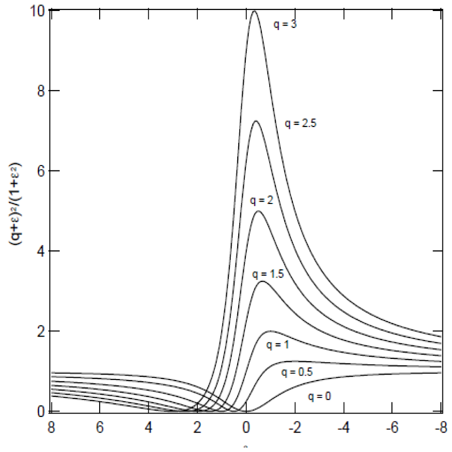

Figure 2.7: Effect of Fano q-parameter on ResPES intensity.

where the left part of the matrix element is the transition rate for normal photoemission from ground (g) to final state (f), the right part is the sum of a direct photoemission term and a set of threshold terms over the possible intermediate state (m) and Γ_m is the lifetime of excited state. V_r and V_A are the radiative (dipole) and the Coulomb (Auger) operators. Under simple assumptions (only one core-hole excitation and a continuum of empty states) this formula can be simplified in the Fano formalism$^{(80)}$, obtaining:

$$\omega = \sum_m |\langle f|V_r|g\rangle|^2 \frac{(q+\varepsilon)^2}{1+\varepsilon^2} \frac{E_m/\pi}{(E_f+E_g-E_m)^2+\Gamma_m} \tag{2.7}$$

where the ResPES intensity is the normal VPES one multiplied by the factor $(q+\varepsilon)^2/(1+\varepsilon^2)$ with $\varepsilon = (E-E_m)/\Gamma$. The parameter q is called *Fano factor* and describes an antiresonant effect for $q = 0$ and an high resonant effect for high $q > 2$, as can be seen in Fig. 2.7. In the case of transition metals (TM) and rare earths (RE) the q factor can be rather high ($q > 3$), leading to a pronounced resonance effect called “giant resonance”.

In the case of Mn over a $Ge(111)$, a clear resonance effect is seen below the absorption maximum. We have shown the onset of on-resonance spectra is different in shape and overall intensity from the off-resonance spectra. The difference between on-resonance and off-resonance spectrum has been termed as Resonant Spectral Weight (RSW). We have traced out the onset of true auger channel after decaying the Raman auger channel in Mn_5Ge_3 system by suitable fitting the valence band spectra for each photon energies as shown in figure 4.5 of chapter 4. A ResPES study of the valence band spectra of Mn:GaSe(0001)interface is described in chapter 5 of this thesis.

Charge transfer time may depend on the intermediate state as referred from Ref.(79). This is due to the excitations into orbitals hybridized with the neighboring atoms, which have higher probability of delocalizing in a given time. On the other hand, close to the threshold, the core-hole decay time has to be replaced by an effective scattering time, which depends on the photon energy relative to the absorption edge(76,77). This effective scattering time can be extracted from the resonant scattering amplitude, described in the Kramers-Heisenberg formulation(75,76) as it will be shown in the following. If we consider the excitation by an incoming photon of energy E_g of an atom from its ground state $|g\rangle$ to all possible intermediate levels $|m\rangle$ of energies E_m and the subsequent decay to a final state $|f\rangle$, the resonant scattering amplitude is given by(75,76)

$$F_{resonance} = \sum_m \frac{\langle f|V_A|m\rangle\langle m|V_r|g\rangle}{E_g - E_m - i\Gamma_m} \tag{2.8}$$

Defining the detuning, Ω, as the energy difference E_g -E_m, one can obtain a scattering time or (effective duration of scattering), following the theoretical explanation from Gelmukhanov and Agren et. al. from ref(76,77)

$$\tau_{CT} = \frac{1}{\Omega^2 + \Gamma_m^2}^{1/2} \tag{2.9}$$

where the contribution to resonant scattering is mostly limited to times τ_{CT}. It is seen that for zero detuning, namely on the resonance, the effective scattering time is given by the core-hole lifetime Γ_m^{-1}, whereas the scattering gets faster for larger detuning. It follows immediately that the probability of observing coherent excitation and deexcitation steps increases with detuning, purely on a quantum mechanical basis as the system will not have sufficient time for relaxation for scattering faster than the charge transfer. In chapter 4, a detailed resonant photo electron spectroscopy on a ordered Mn_5Ge_3 surface has been described.

2.5 Parameterized Configuration Integration Calculations

Many 3d transition metal impurities in semiconductor such as Mn in CdTe or GaAs occupy an intermediate position between two limiting cases. One is the strong localized limit as described by "ligand field theory", and other one is the weak correlation limit as described by "one electron theory". Considering the two descriptions, the Anderson-Impurity model takes into account both the localized states and itinerant band states hybridizing with each other and is suitable to study intermediate cases(68,69). The Anderson hamiltonian describes the hybridization between the strongly correlated d electrons and the delocalized band electrons of the host semiconductor as :

$$\mathcal{H} = \sum_{\vec{k}\sigma} \varepsilon_{\vec{k}} a^{\dagger}_{\vec{k}\sigma} a_{\vec{k}\sigma} + \sum_{\sigma} E_d a^{\dagger}_{d\sigma} a_{d\sigma} + \sum_{\vec{k}\sigma} \left[V_{\vec{k}d} a^{\dagger}_{\vec{k}\sigma} a_{d\sigma} + V_{d\vec{k}} a^{\dagger}_{d\sigma} a_{\vec{k}\sigma} \right] + U a^{\dagger}_{d\uparrow} a_{d\uparrow} a^{\dagger}_{d\downarrow} a_{d\downarrow} \tag{2.10}$$

where $a^{\dagger}_{\vec{k}\sigma}$ and $a_{\vec{k}\sigma}$ are the creation and annihilation operator of the band electron having the wave vector $\vec{k}$, spin σ and $\varepsilon_{\vec{k}}$ (the energy of the corresponding electron). $a^{\dagger}_{d\sigma}$ and $a_{d\sigma}$ are the creation and annihilation operator of the localized Mn $3d$ electrons and E_d is the energy of the d electrons. The third term shows the hybridization between the localized Mn *3d* electrons and the delocalized band electron , that is, the *p-d* hybridization. The last term is the Coulomb repulsive interaction between the localized *d* electrons, where, U is the Coulomb integral between two *d* electrons.

The configuration-integration (CI) cluster model treats the band electrons as molecular orbitals of the ligand atoms surrounding the transition metal (TM) impurity. By this approximation, the information about the band dispersion is lost, however the local electron correlation around the TM impurities are treated explicitly. Furthermore the $3d^n$ ion multiplet structure and the anisotropy of the hybridization between the TM 3d and ligand p orbitals can be explicitly treated.

When the hybridization term is not large compared to the coulomb interaction U in the Anderson Impurity model, different electronic configurations such as d^n, $d^{n+1}\underline{L}$,... (where $\underline{L}$ represents a ligand hole) configuration can be used as a proper basis set. The ground state of the N electron system can be written as:

$$\Psi^{N}_{GS} = a_1 \left|d^{\,n}\right\rangle \; + \; a_2 \left|d^{\,n+1}\underline{L}\,\right\rangle + \ldots \tag{2.11}$$

where $|d^{\,n}\underline{L}^{\,m}\rangle$ represents the basis of $d^{\,n}\underline{L}^{\,m}$ and $\underline{L}$ denotes a hole in the valence band for the Anderson Impurity model or a hole in the ligand p orbitals in the cluster model. The ligand-to-3d charge transfer energy can be given by $\Delta = E(d^{\,n+1}\underline{L}\,) - E(d^{\,n})$ and the $3d-3d$ Coulomb interaction energy is given by $U = E(d^{\,n-1}) + E(d^{\,n+1}) - 2E(d^{\,n})$ where $E(d^{\,n}\underline{L}^{\,m})$ is the center of gravity of the $d^{\,n}\underline{L}^{\,m}$ multiplet. Alternatively, the charge transfer energy and the Coulomb interaction energies can be defined with respect to the lowest term of each multiplet denoted by Δ_{eff} and U_{eff}. Because of the ligand band width W, the charge transfer energy in the solid state environment is reduced by $W/2$, leading to a new parameter $\delta_{eff} = \Delta_{eff} - W/2$. The multiplet splitting are given in terms of Racah A, B and C parameters$^{(72)}$ or Kanamori parameters u, u', j and j' for the multiplet splitting of the d^n configuration due to intra-atomic Coulomb and exchange interactions$^{(73)}$. The Coulomb energy U and the charge transfer energy Δ from the ligand to TM ions are adjustable parameters of the cluster model. To deduce Δ_{eff} and U_{eff} from U and Δ, one can use Kanamori parameters u, u', j and j' from Racah parameter $B = 0.119$ eV and $C = 0.412$ eV for the Mn^{2+} state$^{(73)}$. The multiplet-averaged $3d-3d$ Coulomb interaction energy U and charge transfer energy Δ for d^n can be given by A-14/9B+7/9C and $\epsilon^0_d - \epsilon_p + nU$, where ϵ^0_d and ϵ_p are the bare energy levels of Mn $3d$ and Ge/Se $4p$ orbitals. Furthermore, the transfer integrals between the ligand and TM ions are defined as $V_{n'}$ for the configuration $d^{n-n'-2}$ and $d^{n-n'-1}$. In our calculation for Mn:Ge(111) and Mn:GaSe(0001) interface system, We consider a tetrahedral MX_4 cluster having point group symmetry T_d, where the Mn $3d$ levels split into orbitals with T_2 (yz, zx, xy) and E ($3z^2 - r^2$, $x^2 - y^2$) symmetry. The transfer integrals V$_{t2}$, V$_e$ between the Mn $3d$ orbitals and ligand molecular orbitals are described in terms of Slater-Koster parameters $(pd\sigma)$ and $(pd\pi)$ defined as

$$\begin{aligned} V_{t2} &= \langle L_{yz} \left|\mathcal{H}\right| d_{yz}\rangle = \langle L_{zx} \left|\mathcal{H}\right| d_{zx}\rangle = \sqrt{4/3(pd\sigma)^2 + 8/9(pd\pi)^2} \\ V_e &= \langle L_{x^2-y^2} \left|\mathcal{H}\right| d_{x^2-y^2}\rangle = \langle L_{3z^2-r^2} \left|\mathcal{H}\right| d_{3z^2-r^2}\rangle = 2\sqrt{6}/3(pd\pi) \end{aligned}$$

here, V_{t2} is composed as $V^{\sigma}_{t2} = \frac{2\sqrt{3}}{3}(pd\sigma)$ and $V^{\pi}_{t2} = \frac{2\sqrt{2}}{3}(pd\pi)$.

Using the above parameters, the Hamiltoinan of the Configuration Integration (CI) cluster model is given as

$$\mathcal{H}_i = \begin{pmatrix} E_n + C_n^0 & V_1 & 0 & \dots \\ V_1 & (E_n + \Delta) + C_{n+1}^1 & V_2 & \dots \\ 0 & V_2 & (E_n + 2\Delta + U) + C_{n+2}^2 & \dots \\ \vdots & \vdots & \vdots & \ddots \end{pmatrix} \tag{2.12}$$

Here C_{n+m}^m represents the Coulomb and exchange matrix for the $d^{\,n+m}\underline{L}^{\,m}$ configuration. The ground state energy and the corresponding wave function $|\Psi_{GS}\rangle$ E_0(N) are obtained by diagonalizing the matrix of equation 2.12. The $(N-1)$ electron final states of the photoemission process can be written as:

$$\Psi_{f,i}^{N-1} = b_{1,i}\left|d^{\,n-1}\right\rangle \; + \; b_{2,i}\,|d^{\,n}\underline{L}\,\rangle + \dots \tag{2.13}$$

The Hamiltonian for the final state is given by

$$\begin{pmatrix} E_{n-1} + C_{n-1}^0 & V_1' & 0 & \dots \\ V_1' & (E_{n-1} + \Delta - U) + C_n^1 & V_2' & \dots \\ 0 & V_2' & (E_n + 2\Delta + U) + C_{n+1}^2 & \dots \\ \vdots & \vdots & \vdots & \ddots \end{pmatrix} \tag{2.14}$$

where,$V_{n'}'$ represents the transfer integral between $d^{\,m+n'-2}\underline{L}^{\,n'}$ and $d^{\,m+n'-1}\underline{L}^{\,n'-1}$. The energy and the wave function of the final state are obtained by diagonalizing the above Hamiltonian2.14.

The intensities of the photoemission spectra within this model are given by the transition matrix element between initial and final states, defined by T_{ij}. If we assume $T_{ij} = T =$ constant, the photoemission intensity in a photoemission experiment is calculated, in the sudden approximation, by projecting the final state configurations ($|\Psi_{f,i}^{N-1}\rangle$) onto the ground state$|\Psi_{GS}\rangle$, i.e.can be written as

$$I(BE) \propto \sum_i \left|\langle\, \Psi_{GS}\; |\Psi_{f,i}^{N-1}\rangle\,\right|^2 \delta(BE-\epsilon_i) = \sum_i |a_1 b_{1,i} + a_2 b_{2,i} + \dots|^2\, \delta(BE-\epsilon_i) \tag{2.15}$$

where sum is run over all final state configurations $|\Psi_{f,i}^{N-1}\rangle$ with energy ϵ_i .

A similar approach can be used to calculate the TM core level photoemission spectra. If Q is defined as the interaction between the core hole and the electrons transferred from the ligand to TM cation, the charge transfer energy is replaced by $\Delta - Q$ after the core hole production. The wave function of the final state of the core hole can be written as

$$\Psi_f^{N-1} = c_1 \left|\underline{c}d^{\,n}\right\rangle \; + \; c_2 \left|\underline{c}d^{\,n+1}\underline{L}\right\rangle + \dots \tag{2.16}$$

where, $\underline{c}$ is the core-hole and the hamiltonian can be given by

$$\begin{pmatrix} E_n^c + C_n^{c,0} & V_1^c & 0 & \dots \\ V_1^c & (E_n^c + \Delta - Q) + C_{n+1}^{c,1} & V_2^c & \dots \\ 0 & V_2^c & (E_n + 2\Delta - 2Q + U) + C_{n+2}^{c,2} & \dots \\ \vdots & \vdots & \vdots & \ddots \end{pmatrix} \tag{2.17}$$

where, $E_n^c = E(\underline{c}\,d^{\,n})$ and $X_{n+m}^{c,m}$ are the Coulomb and exchange matrix elements for the $\underline{c}d^{\,n+m}\underline{L}^{\,n+m}$ configuration.

The Mn2p core level photoemission spectra calculation have been carried out in chapters 3, 4 and 5. On the basis of Δ, Q and $(pd\sigma)$ parameterized values, one can estimate the exchange constant $N\beta$ between the Mn^{2+} and the electrons at the top of the valence band of the host semiconductor$^{(74)}$. Considering the second order perturbation with respect to the charge transfer 2.10 we can find

$$N\beta = -\frac{16}{S}\left(\frac{1}{-\delta_{eff} + U_{eff}} + \frac{1}{-\delta_{eff}}\right)\left(\frac{1}{3}(pd\sigma) - \frac{2\sqrt{3}}{9}(pd\pi)\right)^2 \tag{2.18}$$

We have obtained values of Δ, Q, U and $(pd\sigma)$ from the core and valence band spectra for the Mn-doped Ge(111) DMS interface in chapter 3 and Mn-doped ϵ-type GaSe(0001) in chapter 5 respectively.

Chapter 3

Electronic and Magnetic Properties of the Mn_xGe_{1-x} DMS

The electronic and magnetic properties of Mn:Ge(111) interfaces have been investigated by photoelectron spectroscopy and SQUID magnetometry. Two different interfaces are considered, namely an ordered, metallic, Mn:Ge(111) interface and a disordered, semiconducting, Mn_xGe_{1-x} surface alloy, that can be regarded as a diluted magnetic semi-conductor (DMS). Through an analysis of the Mn 2p X-ray photoemission core line, it is shown that the former interface can be described by a single-configuration Mn $3d^6$ initial state, while the latter presents satellite features typical of DMS systems such as the II-VI $Cd_{1-x}Mn_xTe$ and the III-V $Ga_{1-x}Mn_xAs$, where also configurations related to ligand-to-metal charge transfer effects should be accounted for. The metallic interface is found to be ferromagnetic up to room temperature, whereas the DMS alloy displays a paramagnetic behavior. This is tentatively ascribed to the low density on Mn ions that hinders the build-up of a long range FM ordering observed in alloys with a higher Mn content.

3.1 Introduction

As mentioned in the thesis Introduction, the Mn-Ge system can span quite different phases, and display both a semiconducting (e.g. the Mn_xGe_{1-x} DMS) or a metallic behavior (e.g. the Mn_5Ge_3 thin overlayers). As Mn is evaporated on the surface of a reconstructed Ge(111) surface, Mn is known to both diffuse through the surface, as in a DMS alloy, and to be involved in the formation of the Mn_5Ge_3 topmost ordered seed layer$^{(38)}$. Inhibiting the formation of this layer represents a way to produce DMS by Mn evaporation as an alternative route to sputtering or Mn implantation techniques.

Most of the X-ray photoemission studies on the electronic structure have been devoted to the metallic phases, while the semiconducting DMS phases have been virtually neglected. Furthermore, for the semiconducting phases an ambiguity is often found in literature, as no details are provided about the oxygen contaminations, that can easily yield a signal representative of a Mn^{2+} ion due to the formation of MnO. Within this frame, we resorted to study the formation of a Mn_xGe_{1-x} diluted system by, one one side, inhibiting the formation of an ordered surface Mn_5Ge_3 alloy, and, on the other side, by carefully checking the presence of oxygen contaminations. Our experiment allowed us to measure the Mn 2p XPS core levels and to estimate the charge transfer, Mott-Hubbard and hybridization energies through a CI analysis of the Mn 2p spectral weight.

3.2 Sample Preparation

The samples have been prepared by e-beam evaporation of Mn contained in a Mo crucible in ultra-high-vacuum conditions, at a base pressure better than $1x10^{-9}$ mbar. The (111) surface of a Ge single crystal has been selected for the growth of the surface alloy. The DMS alloy is obtained by evaporating at room temperature the Mn layer (0.5 ML) on a sputtered Ge(111) surface. The sputtering prevents the formation of an ordered metallic layer as presented in chapter 4 where the metallic ordered Mn_5Ge_3 interface is obtained by annealing at 400 C a Mn layer (5.2 ML) evaporated onto a c(2X8) reconstructed Ge(111) surface. This annealing induces the formation of an ordered surface layer, which can be regarded as the seed layer for the growth of thicker Mn_5Ge_3 thin films. The surface ordering after annealing has been checked by low-energy electron diffraction and favors the formation of a diluted alloy through the diffusion, already at room temperature, of Mn atoms in the Ge host lattice. Great care has been paid to avoid oxygen contaminations, both after Mn deposition and after annealing, as oxygen in known to readily react with Mn to yield MnO, with significant changes in Mn 2p photoemission core level and Mn 2p-3d X-ray absorption line shapes$^{(60)}$. The electronic structure has been probed by core level photoemission spectroscopy, while magnetic properties have been probed by SQUID magnetometry. The photoemission data have been obtained by exciting the sample with the Al kα line of a twin anode X-ray source. The photoemission spectra have been collected by a VG-Scienta R3000 electron spectrometer. Static molar magnetization (Mmol) was measured at 1000 Gauss from 300 K to 2 K with a SQUID Quantum Design Magnetometer. For the metallic sample, magnetization loops in were collected at 50 K for magnetic fields (H) ranging between 0 and ±2000 Gauss.

3.3 Experimental Results and Discussion

3.3.1 Electronic properties:

Figure 3.1-a shows the Mn 2p core line spectrum collected from the ordered surface alloy, with its characteristic spin-orbit split doublet. The Mn $2p_{3/2}$ component is detected at a binding energy (BE) of 638 eV, while the Mn $2p_{1/2}$ component appears at BE=649 eV. This lineshape is quite similar to that measured on a reference thick (0.2 mm) Mn film (see Figure 2-d), obtained by e-beam evaporation on a sputtered silicon substrate. Following Ref(51), the Mn 2p XPS lineshape was calculated on the basis of a single configuration Mn $3d^6$ initial state (Figure 3.1-b). This was done under the assumption that the metallic character of the sample yields a $3d^6$ electron configuration in the outer shell of the Mn ion, i.e. that the overlap between the 3d and 4s/4p bands increases by 1 unit the count of 3d electrons of atomic Mn. This simple approach has already been used for the theoretical analysis of spin-polarized photoemission spectra of Fe, determined from ab-initio wavefunctions for the ionized states of an isolated Fe+ ($3d^7$) atomic ion(61). The results show that the lineshape of Mn 2p can be well described by the present single configuration atomic approach, which fully accounts for multiplet effects arising from the coupling of the core hole with the outer 3d6 electron shell, while the $3d^5$ atomic calculations (Figure 3.1-c) clearly fails in reproducing the main features of the experimental data. As we will show below, a single configuration approach is not suitable to describe the core level photoemission in the diluted alloy, and a larger set of configurations is required to handle the problem. Figure 3.2 shows the Mn 2p core levels of the Mn_xGe_{1-x} DMS. Three spectra are displayed, in order to evidence the depen-

dence of lineshape on annealing processes. The spectrum of the as-deposited film (Figure 3.2-a) shows a manifold of features, ascribed to both metallic Mn and Mn diluted in the Ge lattice. In fact, a comparison with the Mn 2p XPS core line from metallic Mn (Figure 3.2-d) indicates that the M1 and M2 features (marked by dashed vertical lines) can be ascribed to metallic Mn. These features are progressively quenched with annealing treatments (Figure 3.2-b,c), indicating that the annealing induces a diffusion of Mn into the Ge lattice, rather than a clustering of Mn on the Ge(111) surface. After the second annealing treatment (Figure 3.2-c), the spectrum can be described by two broad peaks (A and C) separated by the spin-orbit interaction. The width of each peak is ascribed to disorder effects, related to both surface sputtering effects and diffusion of Mn into the Ge lattice. On the high BE side of these peaks, two satellites are also detectable (B and D). These satellites are often detected in Mn-based DMS, such as $Cd_{1-x}Mn_xTe$ (Figure 3.2-e), $Zn_{1-x}Mn_xS$ and $Ga_{1-x}Mn_xAs$(95,62), and are ascribed to charge transfer effects from the ligand anions (Te, S or As, respectively) to the 3d levels of Mn cations. These effects can be accounted for in the frame of a configuration interaction model where the electronic states involved in the photoemission process are described by a linear combination of several configurations (see, e.g. Ref.(62) and Refs. therein) such as $3d^n$, $3d^{n+1}\underline{L}$, $3d^{n+2}\underline{L}^2$, where L represents a hole in the ligand created by the charge transfer. The ligand-to-3d charge-transfer energy is defined by Δ=E(d^{n+1})-E(d^n). The intensity of B and D satellites varies depending on the charge transfer energy Δ, as well as on the hybridization strength (T) between the p and d orbitals involved in the charge transfer process (here from Ge 4p to Mn 3d). Therefore, the lineshape analysis of the Mn 2p core levels shown in Figure 3.2-c provides an evidence of Mn-Ge hybridization effects for the Mn_xGe_{1-x} DMS compound. A calculation of the Mn 2p spectral weight for a Mn^{2+} impurity in a Ge matrix is shown in Figure 3.3 and compared with the DMS alloy spectrum of Figure 3.2-c. The calculated curve (shaded area) has been obtained by setting D=1.0 eV, the on-site Coulomb repulsion U_{dd} = 3.3 eV, T = 1.0 eV and the Mn 2p-3d coulomb interaction Q_{pd} = 4.4 eV. These findings are consistent with those obtained on Mn-doped DMS(95,62). As expected, the charge transfer energy is rather low as compared to other DMS systems, as it roughly scales with the energy gap of the host crystal, that for Ge is smaller than for CdTe and GaAs.

Therefore, for the Mn_xGe_{1-x} DMS, the observed lineshape indicates that

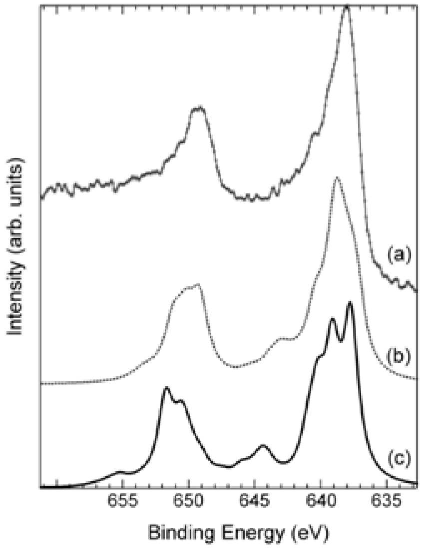

Figure 3.1: Mn 2p core line photoemission spectrum of the Mn:Ge(111) ordered surface alloy (a). Calculated Mn 2p XPS spectra of single-configuration Mn $3d^6$ (b) and Mn $3d^5$ (c) electron systems.

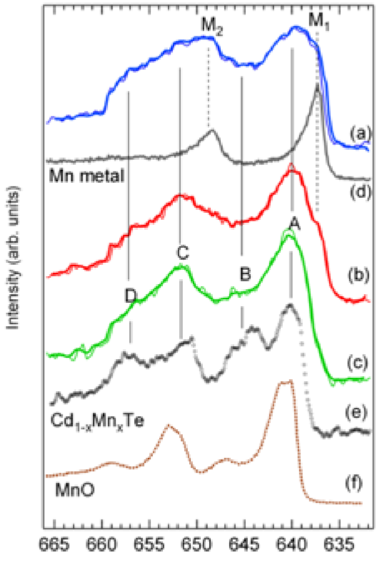

Figure 3.2: Mn 2p XPS spectra of the Mn_xGe_{1-x} DMS. (a) as grown; (b) after the first annealing at 473 K for 15; (c) after the second annealing at 473 K for 30. Mn 2p XPS spectrum of a metallic thick Mn film (d) and of a $Cd_{1-x}Mn_xTe$ DMS [(e), from Ref.(95)].

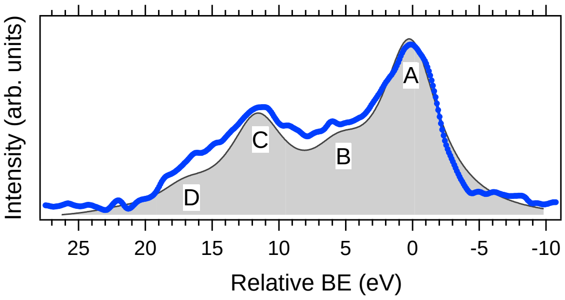

Figure 3.3: Calculated Mn 2p XPS spectrum for a Mn^{2+} impurity in a Ge matrix (shaded area). The calculations are compared to the experimental data obtained from Figure 3.2-c after a Shirley background subtraction (thick line).

charge transfer derived configurations may get some spectral weight and contribute to the final state of the photoemission process, resulting in the observed satellite features B and D in Figure 3.2, similar to those reported for, e.g., $Cd_{1-x}Mn_xTe$ (also shown in Figure 3.2-e for comparison). In turn, the metallic surface alloy virtually shows a single configuration behavior with a fine structure determined by atomic multiplet effects. In principle, the ground state of an itinerant transition metal is assumed to be described by a broad distribution of different d^n weights which converge towards a single d count when electron localization is increased by the effects of U_{dd}. Therefore, in a one-particle model the distribution of the d^n states is given by a binomial distribution that can eventually be modified by electronic correlation effects (see, e.g. Ref.(63), and Refs. therein). Large electronic correlations are supposed to quench charge fluctuations and limit the number of d^n weights. These effects have been invoked to explain the suppression of valence fluctuations observed for the ground state of Mn in MnSi(64).

3.3.2 Magnetic Properties:

The magnetization curves of both samples are shown in Figure 3.4 and Figure 3.5. The ordered surface alloy shows a dependence of magnetization on temperature (Figure 3.4) characteristic of a ferromagnetic ordering established just about 300 K. The inset of Figure 3.4 shows the magnetization loop measured at 50 K. This behavior is consistent with that observed in similar metallic surface alloys(12). For the Mn_xGe_{1-x} DMS, the main features of the M vs. T curve (Figure 3.5) are: (i) an overall Curie-like behavior, revealing the presence of paramagnetic ions (substitutional Mn in the Ge host), (ii) a broad maximum in the 200-250 K range, that could be ascribed to the effects of Mn_5Ge_3 nanoparticle inclusions(65), and (iii) a magnetization increase above 270 K. A similar behavior was observed for $Mn_{0.06}Ge_{0.94}$ thin films grown on a Ge(100) substrate(65). For a higher Mn content, a ferromagnetic behavior is expected, as shown in Ref.(65). The lack of dominant ferromagnetic contribution in the present sample might indicate that the density of Mn atoms diffused into the Ge bulk lattice is still too low to yield a long-range ferromagnetic behavior. It cannot be excluded that the structural disorder (lattice defects, interstitial atoms) induced by sputtering can also hinder the onset of a long-range magnetic ordering. Finally, it is presently not obvious that, if ions with a net magnetic moment are present in the lattice, these moments can align parallel to yield a FM coupling as the alignment also depends on the distance between the magnetic ions.

3.4 Conclusion

We have shown that Mn evaporation on Ge(111) may yield quite different surface alloys, depending on the surface preparation prior to Mn deposition. The difference in surface ordering significantly affects the magnetic and electronic properties. The Mn 2p photoemission core level data provide evidence of Mn-Ge hybridization effects in the DMS alloy. These effects can be accounted for in the frame of a configuration interaction model by assuming charge transfer mechanisms from Ge to Mn. This behavior is quite similar to that observed in other Mn-based DMS(95,62). In turn, the metallic, ferromagnetic surface alloy is virtually described by a single $3d^6$ configuration, suggesting that electronic correlations among 3d electrons are large enough to suppress the 3d charge fluctuations expected in metallic systems. Finally, the lack of a long-range FM ordering in the DMS was tentatively ascribed to the low density of Mn ions, though it cannot be excluded that disorder effects are at work to inhibit the onset of long-range magnetic ordering.

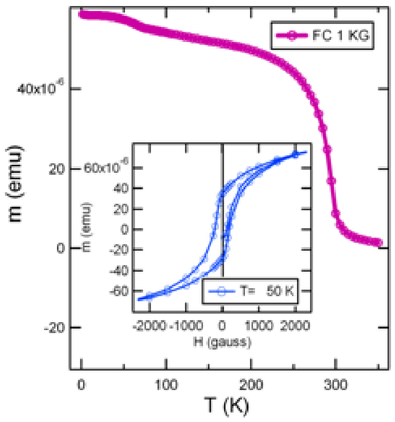

Figure 3.4: M vs. T curve obtained from the ordered surface alloy. The inset shows the hysteresis curve measured at 50 K

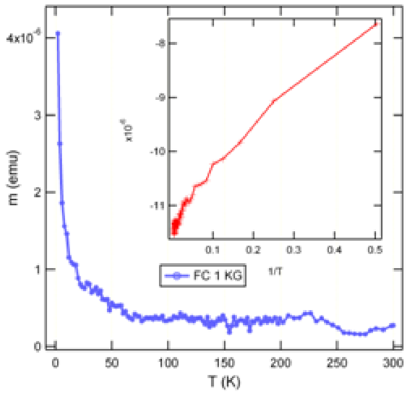

Figure 3.5: M vs. T curve obtained from the Mn_xGe_{1-x} DMS

Chapter 4

Electronic Properties of the Mn_5Ge_3 Ordered Surface

Resonant photoemission from the valence band of $(\sqrt{3}\times\sqrt{3})R30^\circ$ reconstructed Mn:Ge(111) metallic interface has been carried out with the aim to track the transition from resonant Raman to normal Auger emission. The transition energy has been compared with the Mn 2p binding energy, as well as with the Mn L_3 absorption edge energy. Close similarities emerge with respect to the case of elemental Mn thin films, suggesting that the excitation dynamics is dominated by the electronic properties of Mn 3d states, in spite of the bonding with Ge atoms. The switching from the resonant Raman Auger (RRAS) to the normal Auger regime is found about 2 eV below the Mn L_3 absorption edge. A change of the lineshape due to the transition from an overall N-1 electron final state (RRAS channel) to an N-2 electron final state (normal Auger channel) is evidenced by a careful analysis of the experimental data, which also allowed to track the ratio between charge delocalization and core hole timescales as the photon energy is tuned across the Mn L_3 edge. The description of resonant photolectron spectroscopy has been described in chapter 2, in details. However, we will mention below the details from growth followed by characterizations.

4.1 Introduction

The study of excitation dynamics at surfaces and interfaces has greatly profited of resonant electron spectroscopies, in particular for the evaluation of electron charge transfer from absorbed atoms or molecules at the interface with metallic or semiconducting substrates(17,18,19). When a core-valence-valence (CVV) excitation scheme is involved, the dynamics processes become entangled with the direct photoemission channel, yielding the resonant photoemission (RESPES) effect, a well established technique that can provide an element specific probe of the valence band electronic states. In the recent literature, many examples can be found among Mn-based systems, as several experiments have been reported on RESPES at the Mn 2p-3d edge of various oxides (Ref.(20) to(29)), diluted magnetic semiconductors **(DMS)** such as $Cd_{1-x}Mn_xTe$(95), Mn:Ge(111)(12,30) and $Ga_{1-x}Mn_xAs$(40,31), chalcogenides(32,37), molecule-based systems(34,35), and quasicrystals(36). The advantage of using the RESPES techniques is related to the strong enhancement of the 3d electron spectral weight when photoemission experiments are carried out with photons that can excite a *2p* electron to an unoccupied 3d level, leading to a process where two emission channels (direct photoemission and auto ionization) can be simultaneously present and can interfere with each other(41).

In the case of clean (i.e. with no adsorbates) metallic surfaces, the dynamics of excitation in the valence band region occurring when the photon energy is scanned through an absorption threshold has been so far systematically studied, by performing Radiationless Resonant Raman Spectroscopy experiments, on elemental 3d transition metals: Ti(43), V(44), Cr, Fe(42), Mn(45), Ni(46). In general, the tracking of CVV Auger channels is favored by the possibility to carry out experiments at the 2p-3d absorption threshold of the 3d TM atom, which is known to yield giant resonances, as those first observed by Tjeng *et al.* in cuprates(47), due to the enhanced absorption cross section with respect to direct photoemission channel.

The excitation dynamics underlying the ResPES process as the photo energy is scanned through the TM absorption threshold has been described in details in Section 2.4. Here the main concepts are briefly recalled in order to present and discuss the experimental data. In a photoemission experiment, when the exciting photon energy is below the absorption threshold, the normal photoemission channel from valence levels is active, as the photon energy is not high enough to create a core hole. As one approaches the absorption threshold, the autoionization channel is enabled. If the excited electron participates in the decay process, the outgoing electron receives an energy equal to the photon energy and this autoionization channel can interfere with the direct photoemission channel to yield the so-called ResPES or RRAS regime. For higher photon energies the systems turns out to show a normal Auger emission, along with a normal photoemission. In this regime, the excited electron has no relevant interaction with the core hole, and cannot affect the de-excitation dynamics which turns into a normal Auger, two-hole, final state.

In the description of excitation dynamics three reference energies are usually regarded: the binding energy of the core electron (EB), the energy of the absorption threshold (EX), and the energy (EC) at which the cross-over from RRAS to normal Auger emission occurs. The relationships among these energies have been shown for V, Cr, Mn, Ni and Fe(44,42,45).

On the basis of the ResPES data published in Ref.(12), in the present section, we investigate the excitation dynamics for a reconstructed Mn:Ge(111) ultra-thin interface alloy obtained by Mn evaporation on a Ge(111) single crystal surface, with the aim to identify the relationship among EB, EC, and EX. The choice of this interface is motivated by the interest of the Mn-Ge system as a DMS with possible applications in the field of spintronics, as recently reported for the $Mn_{0.05}Ge_{0.95}$ quantum dots(5). Indeed, this system has shown to be a very rich playground for testing spintronic architectures, ranging from the Mn_xGe_{1-x} diluted alloy (x=0.01 to 0.05)(6), to the $MnGe_2$ nanocolumns(7), as well as to a number of Mn:Ge(100) or Mn:Ge(111) interfaces (see, e.g., Ref.(10) and(12)). The latter subsystem is actually that considered in the present study. Here, the excitation dynamics is explored by tracking the energy (binding or kinetics) of several spectral features in the valence band region in a wide photon energy range, including what is observed far above the L_2 threshold. This allows a better identification of the EC point through the crossing of constant with linearly dispersing set of data points.

The RRAS to normal Auger crossover at EC is related to charge delocalization, a key issue of spintronics, as the control over spin, and charge, dynamics is at the root of the potentially new functionalities of spintronics devices(48). Indeed, in the present interface, the excited electron is injected into a spin-polarized band which undergoes a ferromagnetic transition close to room temperature(12,49). Therefore an evaluation of the competing mechanism of charge delocalization and core-hole decay may provide useful information on the dynamics of spin polarized carriers.

4.2 Sample Preparation and Experimental Details

The $(\sqrt{3} \times \sqrt{3})R30°$ reconstructed interface was prepared, as reported in Ref.(12), by evaporating a 4 ML thick Mn film on the (111) surface of the Ge single crystal. Post-growth annealing was carried out from 300 ° C to 500 ° C for 120 seconds to induce the surface alloy formation. In photoemission experiments, the RESPES spectra were collected by scanning the photon energy from $h\nu$=636 to 657 eV through the Mn 2p-3d absorption edge. Additional photoemission spectra were collected with a photon energy of 840 eV, in order to control surface contaminations and estimate the thickness of the annealed layers. The measurements have been performed at the CNR-IOM ALOISA synchrotron beamline in Trieste (Italy)(50).

4.3 Experimental Results and Discussion

Figure 4.1 shows the XAS spectrum measured at the Mn L-edge. The L_3 and L_2 edges are clearly observed, separated by about 10.5 eV. The XAS spectrum is compared with the Mn 2p XPS spectrum collected with a $h\nu$= 840 eV photon energy. Also in this case the two Mn $2p_{3/2}$ and Mn $2p_{1/2}$ spin-orbit split peaks are clearly detectable. While the maximum (EX) of the Mn L_3 band is detected at $h\nu$=640.4 eV, the maximum (EB) of the Mn $2p_{3/2}$ peak is observed at $h\nu$=638.5 eV. This energy difference will be discussed extensively later.

In Figure 4.2, left panel, the resonant photoemission data obtained by scanning the photon energy through the Mn 2p-3d absorption edge are shown. The valence band spectra have been stacked on the vertical axis by a constant height. The red and blue line represent a guide for the eye to track the binding energy of the main spectral features. The bottom spectrum represents the off-resonance spectrum and the spectral shape is dominated by the Ge valence band emission. Nevertheless, a Fermi edge is detectable, due to the surface alloy formation.

In Figure 4.2, right panel, the sequence of photoemission spectra collected across the Mn 2p-3d resonance are displayed after subtracting from each spectrum the off-resonance spectrum collected at $h\nu$=636 eV. In this way only the resonant spectral weight (RSW) is shown. This subtraction procedure is

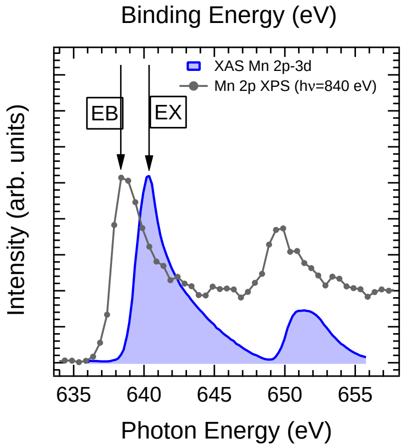

Figure 4.1: Mn 2p XPS core line collected with a hν=840 eV photon energy. The binding energy scale is shown on the top axis. Mn L-edge XAS spectrum$^{(12)}$ (shaded area). The photon energy scale is shown on the bottom axis. EX and EB denote the maximum of the Mn L_3 absorption band and the maximum of the Mn $2p_{3/2}$ XPS peak, respectively.

adopted in order to track the binding energy of the main spectral features without possible distortions induced by the presence of the non-resonant spectral weight contribution.

Before going into the details of the excitation dynamics, in Figure 4.3, a few selected valence band spectra extracted from Figure 4.2, right panel, are shown, with the aim to identify the main spectral features occurring upon the scanning of the photon energy through the Mn L-edge. Figure 4.3-a shows the valence band spectrum collected below the L_3-edge (hν=638.6 eV). In this spectrum a maximum at BE=3 eV can be observed, along with an emission at low BE, which extends up to the Fermi edge. This spectrum can be regarded as dominated by the RRAS emission. Figure 4.3-b shows a valence band spectrum collected with a photon energy (hν=640.4 eV), at the maximum of the L_3 edge. The main peak is now shifted to higher binding energies (BE=5 eV) with respect to the previous case. This spectrum has to be regarded as dominated by the Auger emission that will ultimately end into the normal Auger L_3VV channel (Figure 4.3-c). Finally, Figure 4.3-d shows a VB spectrum collected with a photon energy around the L_2 threshold. In this spectrum both the L_3VV normal Auger at BE=15 eV and the enhanced spectral weight due to L_2VV Auger at BE=4 eV can be detected.

An interpretation of the lineshape of both RRAS and normal Auger emis-

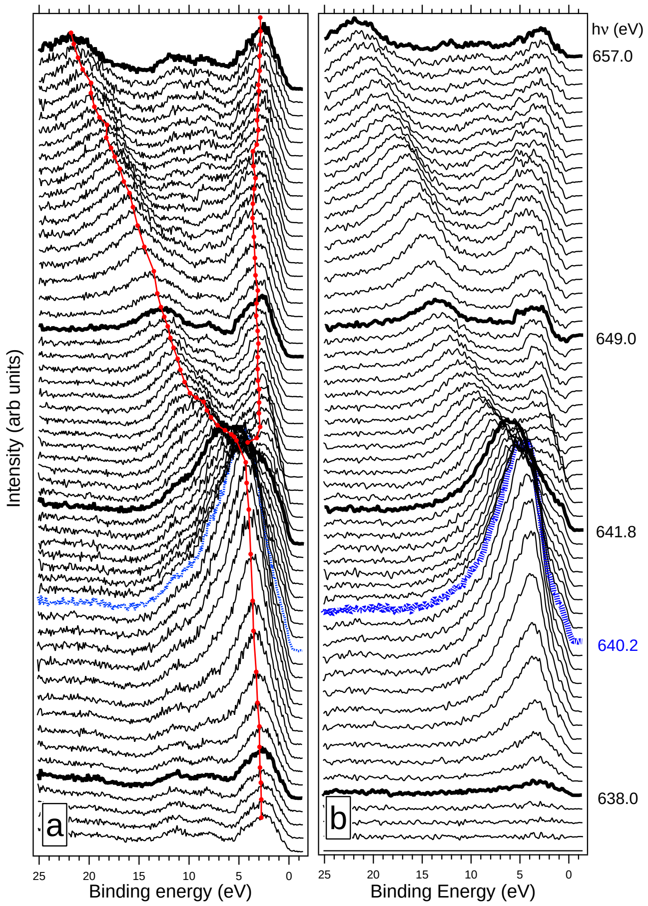

Figure 4.2: (Color online) Left panel: RESPES spectra collected by scanning the photon energy from hν=636 to 657 eV through the Mn 2p-3d absorption threshold (adapted from Ref.$^{(39)}$). The branched line is meant to be a guide for the eye indicating the detectable normal Auger and photoemission channels across the Mn L-edge. Right panel: Resonating spectral weight (RSW) in the valence band obtained by subtracting from each spectrum in the left panel the photoemission spectrum measured off-resonance at 636 eV. In both panels the intensity of each photoemission spectrum is plotted in a 0 to 25 eV binding energy range, while the sequence of photoemission spectra has been collected by sweeping the photon energy from below the Mn L_3 absorption threshold (hν=636 eV) to above the Mn L_2 threshold at hν=657 eV. From 636 to 638 eV, the photon energy step was Δ(hν)=0.5 eV, from 638.2 to 641.8 eV, Δ(hν)=0.2 eV, from 642.5 to 649 eV, Δ(hν)=0.5 eV, and from 649.4 to 657 eV, Δ(hν)=0.4 eV.

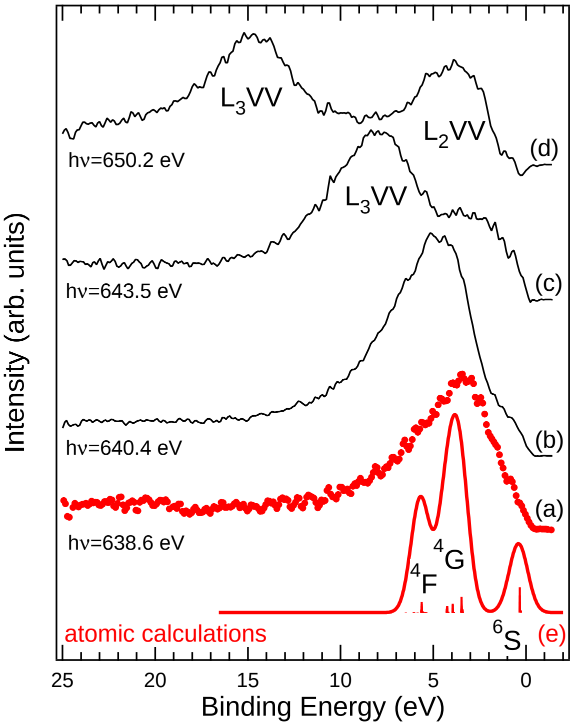

Figure 4.3: Selected RSW spectra collected at different photon energies across to Mn L-threshold. The data are compared with single-configuration atomic calculations of the two-hole one-electron final state (initial state $3d^6$, Ref.(51)).

sion can be carried out at the light of recent investigations on atomic effects in the photoemission of the Mn:Ge(111) interface(51). In the RRAS regime the final state of the system is two-hole one-electron like, whereas in the normal Auger regime it is two-hole like. A simple, though consistent calculation of the electron emission from a Mn:Ge(111) interface can be carried out in the atomic single-configuration limit, by assuming that the initial state of the Mn atom is $3d^6$. In this way the electron delocalization in the intermetallic compound is accounted for by adding one electron to the atomic Mn $3d^5$ configuration, as the 4s and 3d bands overlap in the valence band region. In this frame, the RRAS collected below the L_3 edge is calculated as a $3d^5$ final state, arising from the single configuration $3d^6$ ground state, consistently with the N-2+1 (i.e. 6-2+1) electron count of the autoionization channel.

Therefore, the direct photoemission channel is described as: $2p^6 3d^6 + h\nu \rightarrow 2p^6 3d^5 + e_k$, whereas the autoionization channel includes the Mn 2p-3d photo-absorption, followed by the 3d-2p decay and the 3d electron emission: $2p^63d^6 + h\nu \rightarrow 2p^53d^7 \rightarrow 2p^63d^5 + e_k$. The difference between the RRAS and the RAE is related to the role of the 3d electrons in the decay process. The intermediate state of the autoionization process can be formulated as $2p^5[3d^6, \overline{3d}^1]$, where $\overline{3d}^1$ labels the electron excited into the unoccupied 3d levels by photoabsorption. If this electron participates in the decay process by filling the 2p core hole, the final state is $[2p^5, \overline{2p}^1]3d^5 + e_k$, while in the case of the spectator decay, one has a $2p^6[3d^4, \overline{3d}^1] + e_k$ final state. In turn, the normal Auger emission is a two-hole final state and assuming the $3d^6$ initial state for the Mn ion in the intermetallic alloy, the Auger process can be described as $2p^63d^6 + h\nu \rightarrow 2p^53d^6 + e_k \rightarrow 2p^63d^4 + e_k + e_{k'}$.

The results of the atomic calculation are shown in Figure 4.3-e (thick line). Here the computational results are regarded as an aid to discuss the origin of the spectral features emerging from the analysis of the experimental data. The calculated Mn spectral weight in the valence band results to be composed of a set of three peaks, labeled according to the prevalent term contributing to each of them, namely ^{4}F, ^{4}G and ^{6}S in the L-S coupling scheme notation. This single-configuration calculation catches the main features of the RRAS spectrum (Figure 4.3-a). The calculated low-BE ^{6}S peak can account for the resonating spectral weight close to the Fermi level, the ^{4}G central peak accounts for the maximum observed in the RRAS spectrum, though the measured BE is about 1 eV lower, and the calculated ^{4}F peak can account for the spectral weight observed on the high BE side (i.e. BE > 5 eV) of the RRAS maximum. The atomic calculations have been carried out for an isolated Mn atom and therefore discrepancies with respect to the experimental data can be expected, since the solid state effects on the Mn atom, and in particular possible distortions of the atomic spherical symmetry due to the local crystal structure around the Mn ion, have not been considered. An improvement of the agreement between calculations and experimental data, both in terms of energy separation and relative intensity of the calculated multiplet spectral features is therefore expected when the effects of solid state environment mentioned above are considered.

The RRAS spectrum is in principle different from the two-hole satellite (normal Auger), as a different multiplet is expected from the $3d^4$ (N-2 electron) final state of the Auger process. In spite of the width of the spectral features, this seems to be confirmed by a comparison of the (a) and (d) spectra of Figure 4.3, as the RSW in the RRAS regime shows a different lineshape

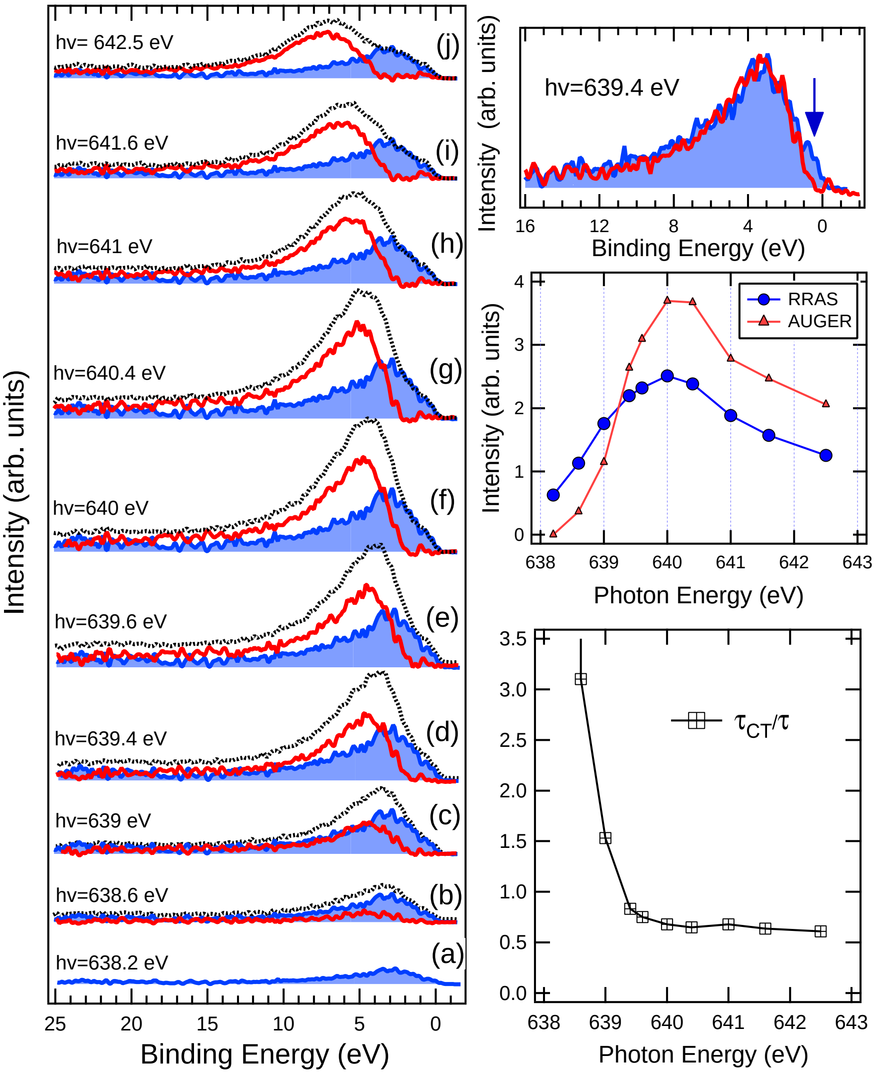

Figure 4.4: Left panel: Selected RSW spectra (dashed lines) collected at different photon energies across to Mn L-threshold. For each spectrum the normal Auger contribution (red line) and the RRAS contribution (shaded blue area) are shown. Right panel: RRAS and Auger emission measured at hν=639.4 eV. The Auger spectrum has been shifted to low BE and scaled to match the maximum of the RRAS spectrum; photon energy dependence of the RRAS (I_R, filled circles) and normal Auger (I_A, filled triangles) spectral weights (i.e. integrated intensities), as well as of the τ_{CT}/τ ratio (open squares). The thin lines are drawn as a guide for the eyes.

with respect to the L_3VV Auger emission. The main difference is determined by the feature on the low-BE side of the RRAS spectrum (i.e. the emission, labeled as ^{6}S, according to the atomic calculations, at the Fermi edge). This difference will be confirmed by a direct comparison presented in Figure 4.4, right panel.

The possibility to track both the normal Auger emission and the RRAS emission at photon energies above the L_3 threshold suggests the coexistence of both channels above the ionization threshold, as already shown in the case of the insulating $CuGeO_3$(53). To further investigate this issue, we have carried out a data analysis based on the assumption that each RSW spectrum of Figure 4.2-b can be decomposed into the sum of RRAS and normal Auger contributions. Therefore we have subtracted from selected RSW spectra the RRAS spectrum measured at 638.2 eV. The results are reported in Figure 4.4 (left panel), where the RSW spectra (dashed lines) are shown along with the normal Auger (thin line) and RRAS (shaded area) emissions. For the spectrum at 638.2 eV (Figure 4.4-a) only the RRAS contribution is considered. As the photon energy increases, the normal Auger emission is seen to emerge and finally dominate the spectral weight at the L_3 edge (Figure 4.4-d). Consistently, the Auger component shows a BE shift as the photon energy increases, while the RRAS BE is fixed. This analysis also indicates that the two components (RRAS and Auger) have different lineshapes, as can be observed in the top-right panel, where the BE shifted Auger spectrum and the RRAS spectrum detected at hv=639.4 V have been superposed. As previously observed in the comments to Fig.4.3, the main difference between the two spectra is found in the low binding energy region (indicated by the vertical arrow in Figure 4.4, right panel), where the emission labeled as ^6S has been identified.

Following Ref.(18), it is possible to evaluate the ratio between the charge delocalization time and the core-hole lifetime. This evaluation is often carried out to study the charge transfer dynamics occurring in the femtosecond regime across various interfaces, including molecule/metal, molecule/semiconductor and molecule/molecule interfaces. This approach, based on resonant photoemission spectroscopy, is often mentioned as the core-hole clock technique in the field of atomic, molecular and interface physics(54). Provided that it is possible to estimate the intensity I_R of the RRAS and I_A of the normal Auger emissions, the ratio between the respective time constants is(54) $\tau_{CT}/\tau = f/(1-f)$, where $f = I_R/(I_R+I_A) = I_R/I_{total}$. In the present study,

τ_{CT} is not the time scale of a charge transfer processes from the adsorbate to the substrate, but it should be regarded as the delocalization time of the electron excited in the intermediate step of the autoionization process. This estimation is rather difficult in condensed phase systems, due to the intrinsic band broadening of energy levels involved in both the normal Auger and RRAS emissions. Because of this broadening, the two channels often overlap with a rather featureless lineshape. However, the present data shows that, upon careful analysis, the ratio can be calculated, providing an estimation of the time scales on the excitation dynamics. Therefore in Figure 4.4 (right panels) we show, as first, the dependence of I_R and I_A on photon energy, and then we derive from these intensities the estimated τ_{CT}/τ, ratio. As can be observed, τ_{CT}/τ decreases as the photon energy increases. In particular, at about $h\nu$=639.2 eV I_R and I_A have a comparable weight and τ_{CT}/τ=1. Above this photon energy, the Auger channel prevails as the delocalization time decreases with respect to the core-hole lifetime (i.e. the delocalization process becomes faster) and therefore the probability for the excited electron to participate in the autoionization process is reduced. In order to provide a first justification of these results, following Mentes *et al.* (Eq.2 and Eq.3 of Ref.(20)), we approximate the charge transfer time as $\tau_{CT} = 1/(\Omega^2 + \Gamma^2)^{1/2}$, where $\Omega = h\nu - \langle E_{3d} \rangle$ represents the detuning energy, i.e. the energy difference between the photon energy hν and the average energy $\langle E_{3d} \rangle$ of the set of unoccupied 3d levels that can be reached by the absorption process, and Γ is the core hole lifetime width at the resonance. As $\Gamma \sim \tau^{-1}$, we can predict a decrease of τ_{CT}/τ with the photon energy since τ_{CT}/τ results to roughly scale as $[h\nu - \langle E_{3d} \rangle]^{-1}$. Indeed, we observe a τ_{CT}/τ decrease, with a nearly fourfold reduction as the photon energy increases from 638.6 eV to the maximum EX of the absorption band at 640.4 eV.

Finally, we consider the energy dependence on photon energy of the emission channel so far considered. Figure 4.5, bottom panel, shows the binding energy of the RSW as the photon energy is scanned across the Mn L-edge. We considered only the maximum of the intensity of the valence band region. The BE is displayed on the vertical axis, while on the horizontal axis the photon energies are reported. Slight differences are detected between the tracking performed on the spectra with and without the subtraction of the off-resonance contribution. The energy of the Mn 2p core level (EB=638.5 eV) and that of the Mn L_3 threshold (EX=640.4 eV) are indicated by the vertical arrows. The energy EC of the RRAS to Auger transition is determined as the crossing point after linear interpolation of the constant BE (normal and resonant photoemission behavior) and the normal Auger emission channels. Depending on the data-set used to track the energy dispersion of the states, the cross-point (EC) is set at 638.4 eV if the constant binding energy states are extracted from Figure 4.2, left panel, while EC=638.8 eV, if the RSW data are used (Figure 4.2, right panel). We regard the latter estimation, based on the RSW, more reliable than the former, as the subtraction of the non-resonating spectral weight is meant to reduce the effect of possible systematic errors.

The data in the inset of Figure 4.5 confirms the differences between the RRAS and the normal Auger behavior. Indeed, while the RSW intensity (open circles) is already present at about 649 eV, the normal Auger intensity (filled squares) is larger than the RRAS contribution above about 650 eV. Here the different intensities are unambiguously tracked, as the RRAS is well separated from the normal Auger emission, while at the Mn L_3 edge, a clear separation between the two channels was not apparently detectable. However, the analysis of Figure 4.4, right panel, shows an energy dependence of the RRAS and normal Auger intensities consistent with that presented in the inset of Figure 4.5.

The results are summarized in Table 4.1, which also reports a comparison with the results obtained from elemental metals. In Table I the values of EX-EB, of the L_3VV emission relative to E_F, and of the RRAS-AUGER crossover (i.e. EC-EB) obtained from the present analysis are indicated, along with those reported for elemental TM surfaces (adapted from Ref.(45)). As can be observed, the excitation dynamics of the present reconstructed, metallic, Mn:Ge(111) interface is quite similar to that observed for an elemental Mn thin film, showing that, in spite of the intermetallic nature of Mn:Ge(111) the excitation dynamics is dominated by Mn electronic states.

This fact can be explained on the basis of the surface structure of the Mn_5Ge_3 ultra-thin film grown on Ge(111). Several scanning tunneling microscopy studies have provided the evidence of two protrusions in each surface unit cell arranged in a honeycomb pattern(10,55). Theoretical approaches on the surface electronic structure have predicted that these protrusions could be ascribed to Mn atoms on top of the $Mn_5Ge_3(0001)$ surface(10,56). These atoms are usually labeled as Mn_I atoms, according to the crystal structure proposed by Forsyth and Brown(57), while Mn_{II} atoms are located on the subsurface layer and make bonds with Ge atoms. Recent scanning tunnel-

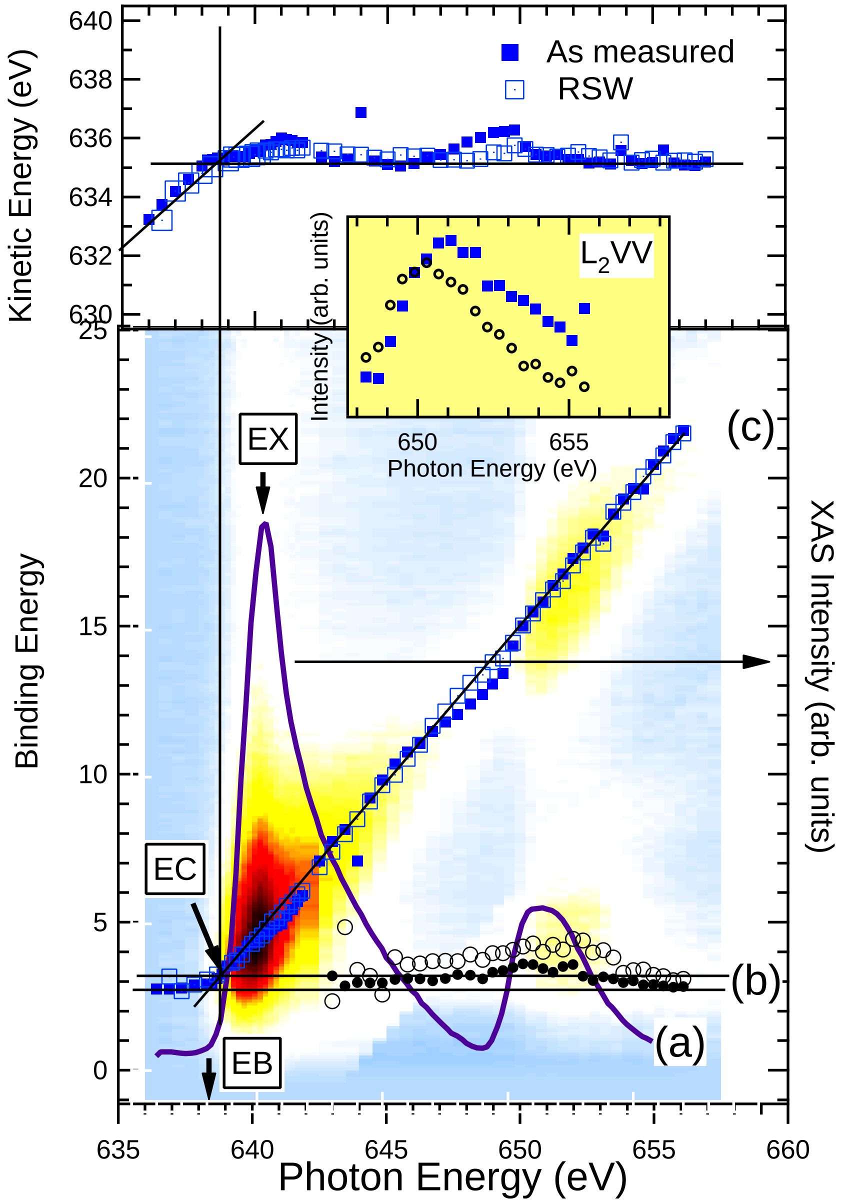

Figure 4.5: Bottom panel: Mn 2p-3d XAS spectrum (a), tracking of the peak intensities of the constant binding energy feature at 3 eV (b), and of the constant KE energy feature (c). The density plot in the background represents the RSW displayed in Figure 4.2-b, as a function of both photon energy and binding energy. Top panel: tracking of the two-hole peak energies as a function of the kinetic energy. Open symbols indicate the RSW, while filled symbols the as-measured data. Inset: detail of the RSW profile (circles) scanned across the Mn L_2 edge and of the CVV Auger transition intensity (squares) in the same energy range

Table 4.1: L_3VV Auger decay parameters of 3d transition metals and compounds. Data of Mn:Ge(111) are extracted from the present experiments. The data for the other systems are taken from Ref. (45). EX is the energy of the peak of the Mn L_3 threshold, EB is the binding energy of the Mn 2p photoemission peak, EC is the energy of the cross-over between the RRAS and normal Auger regime.

	EX-EB	L_3VV emission relative to E_f	RRAS-AUGER crossover (EC-EB)
V	3.0	2.3	0.0
Cr	2.0	3.5	0.0
Mn	1.6	3.3	-0.1
$Mn : Ge(111)$	1.9	3.2	0.3
Fe	0.9	3.2	-1.0
Ni	0.0	6.0	0.0

ing spectroscopy studies combined with angle-resolved photoelectron spectroscopy (58), have provided an experimental evidence of the theoretical predictions, ascribing specific electronic states close to the Fermi level to the topmost Mn_I atoms in the honeycomb lattice. This could explain the present evidence of an electron dynamics dominated by Mn states. It is worth mentioning that also band structure calculations for bulk Mn_5Ge_3 have predicted a relevant contribution of manganese states in the 0-3 eV BE region. In particular, the lowest lying states at BE=0.7 eV were ascribed Mn_I atoms (59).

4.1 Table 4.1 also shows that EX is larger than EB, as already observed in Cr, Fe, and V. Following Ref. (42), we ascribe the energy difference between EX and EB to the correlation energy in the open-shell 3d electron system. In fact, when an electron is excited from the transition metal 2p core level to the 3d shell upon photon absorption, this electron adds to a correlated electronic state (from 6 to 7 electrons in the present case) and the extra (correlation) energy has to be supplied by the incoming photon energy.

4.4 Conclusion

We have carefully analyzed the resonant photoemission data reported for a $(\sqrt{3} \times \sqrt{3})$R30° reconstructed Mn:Ge(111) interface$^{(12)}$ with the aim to track the electron excitation dynamics across the Mn L-edge. A resonant enhancement of the valence band has been observed for photon energies hν lower than the 2p absorption maximum (radiationless resonance Raman spectroscopy, RRAS). For larger photon energies a normal Auger transition is observed, which is identified from its constant kinetic energy. The switching between the RRAS and the normal Auger regime is found to occur less than 2 eV below the transition metal L_3 edge, a behavior recently found in metallic Mn thin films$^{(45)}$. This energy difference is directly probed by the behavior of the RRAS and normal Auger intensities across the Mn L_2 threshold. Finally, it is shown that the RRAS and normal Auger emission can coexist above the ionization threshold and have different lineshapes, according to different multiplets expected for the N-1 and N-2 final states. In spite of the rather broad bands related to the RRAS and normal Auger emissions, the RSW at the Mn L_3 edge has been decomposed into the sum of the RRAS and normal Auger contributions, which allowed to track the ratio between the time scale of charge delocalization and of the core hole lifetime as a function of the photon energy.

We believe that the analysis on charge transfer dynamics proposed in the present study could be extended to other systems. As an example, we wish to mention that the resonating emission close to the Fermi edge observed in the Mn_5Ge_3 RRAS spectrum, is apparently present also for RRAS in Cr (Figure 3 of Ref.$^{(42)}$), indicating that the RRAS can have distinctive features that make it different from the normal Auger emission. In fact, also for the case of Cr, while a clear Auger emission is detected at 3.5 eV on the BE scale, a constant BE feature is detectable at the Fermi edge. On resonance, this feature seems to show the maximum intensity, while appears to be quenched well above resonance.

Finally, as for the dynamics of carries injected into the empty levels of the Mn_5Ge_3 conduction band, we can provide useful information on the characteristic energy and time scales. As first, our results show that(i) electronic states with significant Mn contribution are present at the Fermi level, with a high spin ^{6}S multiplet term in the final state of the photoemission process. (ii) When the charge is injected, the tracking of τ_{CT}/τ ratio as the photon energy approaches the absorption threshold, indicates a nearly four-fold decrease of the delocalization time τ_{CT} with respect to the 2p hole lifetime τ in an energy range of about 1.8 eV. (iii) When electrons are excited into the 3d empty states, following photon absorption at the Mn L-edge, an extra correlation energy of about 2 eV is required to set up the N+1 final state of the absorption process. This could be assumed as an estimate for the energy involved in a charge injection process into the partially filled 3d shell.

Chapter 5

Electronic structure and magnetism of the Mn:GaSe Interface

5.1 Introduction

In this chapter, we present a study aimed to grow a $Ga_{1-x}Mn_xSe$ surface alloy by e-beam evaporation of Mn on a freshly cleaved ε-type GaSe(0001) surface and to explore its magnetic properties and their relationship with the local electronic structure. SQUID magnetometry, X-ray core level photoemission and soft X-ray absorption spectroscopies are combined to address the origin of the observed magnetic behavior.

There are several GaSe polytypes which differ in the stacking sequence of the basis layer units of the three most important β-GaSe, ϵ-GaSe, and γ-GaSe are shown in Figure 5.1. In addtion to these polytypes, one has to consider possible segregations in the Mn-Ga-Se system. Indeed, bulk crystal phases like $MnSe_2$ (cubic pyrite structure), α-MnSe, β-MnSe, $MnGa_2Se_4$ and interfaces of Mn with Ga-Se compounds like Ga_2Se_3 displaying topmost segregation of rocksalt MnSe layers have already been known(85).

Two kinds of samples based on Mn-doped on GaSe(0001) have been considered in this thesis. In the first sample, the Ga substitution with Mn occurring upon deposition at RT of Mn on GaSe(0001) has been addressed, while, in the second sample, annealing effect have been considered to trigger further diffusion of Mn in the GaSe lattice. While in the first case we have

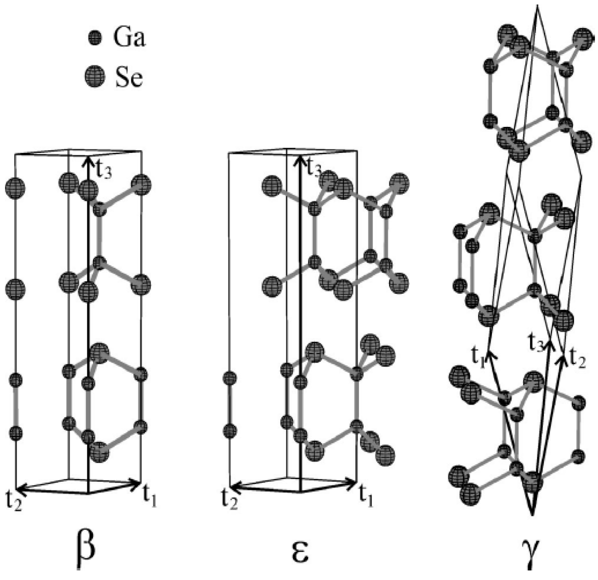

Figure 5.1: Unit primitive cells for left β-GaSe, ϵ-GaSe middle and γ-GaSe right taken from ref.$^{(83)}$.

explored a wide range of Mn coverages, in the second case, the deposition was kept below the threshold of metallic Mn segregation on the surface. Electron spectroscopies (including synchrotron based techniques) have been used to study the electronic structure of the undoped and Mn doped ϵ-GaSe(0001) surfaces.

In Figure 5.2, we show an image of the as-received ϵ-GaSe single crystals. As these crystals constitute stack of Ga or Se layers weakly bonded by van der Wall's interactions, it has been possible to cleave the surface inside the vacuum chamber and prepare a clean flat surface for UHV experiments. The cleaving of the surface has been done by applying a horizontally slash on to the tip attached over the GaSe sample, which breaks the van der wall's interactions between the Ga or Se stacking layers. The tip takes away the attached part of GaSe sample and leaves a clean flat surface of GaSe.

A top view representation of the GaSe(0001) surface is shown in figure 5.3, where t_1 and t_2 are the primitive vectors. The GaSe(0001) surface has a threefold rotational symmetry and so the Γ-M and Γ-M' directions are nonequivalent. Angle resolved photoelectron spectroscopy (ARPES) studies on the undoped GaSe (0001) are presented in Ref.$^{(83)}$.

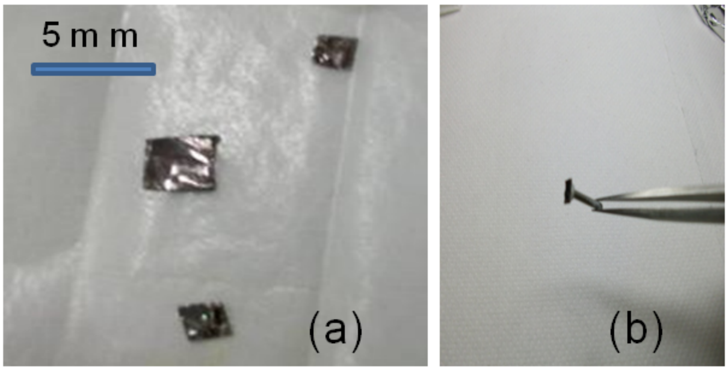

Figure 5.2: (a) A pictorial image of ϵ-GaSe single crystal; (b) A pin attached over the single crystal to be cleaved inside the vacuum chamber

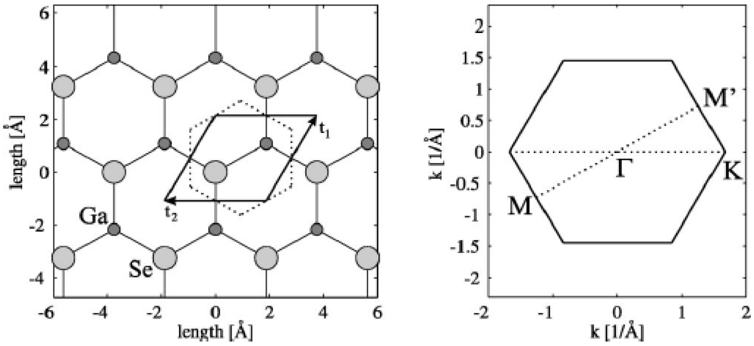

Figure 5.3: Left: top view of the GaSe(0001) surface. The primitive hexagonal cell is indicated by dotted lines and the primitive cell used in the band structure calculations of ϵ and β GaSe by a solid line. Right: the corresponding Brillouin zone with M and $\acute{M}$ points indicated taken from ref.$^{(83)}$.

5.2 Growth of Mn layers on ϵ-type GaSe(0001)

5.2.1 Multiple Deposition of Mn on ϵ-type GaSe(0001)

The $Mn - GaSe$ interfaces have been obtained by evaporating Mn ions with an e-beam evaporator on the ϵ-GaSe (0001) surface of UHV-cleaved single crystals. Up to nine successive depositions of Mn on a freshly cleaved ϵ-GaSe(0001) single crystals have been carried out, each deposition lasting 20 seconds at a constant flux of 500 nA. An Omicron electron-beam evaporator was used, equipped with a Mo crucible containing Mn flakes.

Atomic Force Microscope (AFM) imaging of both clean and as grown interface have been carried out with a NT-MDT P47 AFM probe. Some of the results for the clean surface and the surface obtained after the ninth Mn evaporation are shown in Figure 5.4 and 5.5, respectively. In Figure 5.4, the left panel shows the 2D AFM image ($1\mu m$ x $1\mu m$) of a clean ϵ-GaSe(0001) surface cleaved in ultra high vacuum. The right panel depicts a horizontal line profile taken from the 2D AFM image. In the right panel, the spacing between horizontal and vertical lines is 0.2 nm and 0.2 μm, respectively. The average roughness calculated from the 2D image is 1.74 ± 0.31 nm.

In turn ,in the Mn-doped GaSe surface some clusters appear in the 2D (1 μm X 1 μ m) AFM image (left panel) of the figure 5.5. The right panel depicts a horizontal line profile showing surface heights of about 15 to 30 nm. In this panel, the spacing between each horizontal or and vertical lines is 5 nm or 0.1 μm, respectively. We ascribe these clusters to Mn atoms that did not diffuse through the surface after the latest evaporations.

To characterize the outcome of the Mn deposition on the surface, we have carried out XPS measurements after each deposition. The intensity of the Mn core levels increases with deposition time. The features ascribed to metallic Mn in the last steps of Mn deposition are also detectable in Figure 5.6. They are marked with a vertical arrow. Normalized Mn core level as well as the shallow core levels (Ga3d, Se3d and Mn3p) are shown in Figure 5.6 and 5.7, respectively.

The intensities of Mn2p, Ga2p, Ga3d, Se3d and Mn3p spectral features collected after each Mn deposition have been obtained by fitting the core lines with a Gaussian wave function. The results are shown in Figure 5.8 and 5.9.

In Figure 5.8, the Ga 2p signal attenuation with deposition time is well

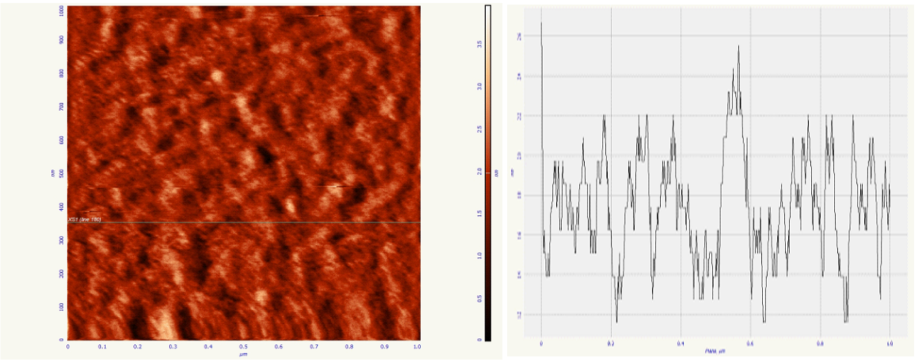

Figure 5.4: 2D AFM image ($1\mu m$ x $1\mu m$) of a clean ϵ-GaSe(0001) surface cleaved in ultra high vacuum(left), horizontal line profile taken from the AFM image where the spacing between horizontal and vertical lines are 0.2 nm and 0.2 μm, respectively (right).

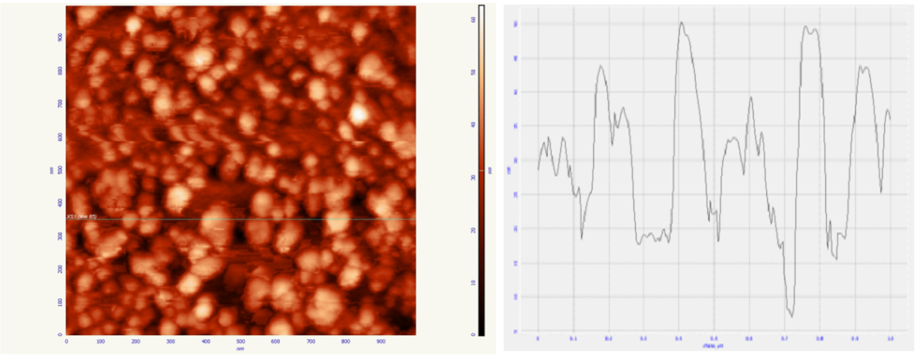

Figure 5.5: 2D AFM image ($1\mu m$ x $1\mu m$) of the Mn-doped on ϵ-GaSe(0001) interface after the last step of Mn deposition at room temperature(left), horizontal line profile taken from the AFM image where the spacing between horizontal and vertical lines are 5 nm and 0.1 μm, respectively (right).

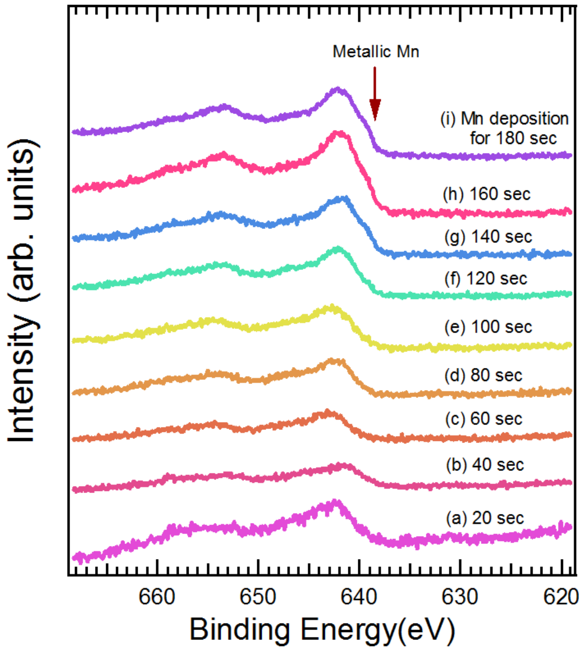

Figure 5.6: Series of Mn 2p spectra collected with Al Kα photon source for Mn deposited in steps on ϵ-GaSe(0001) surface.

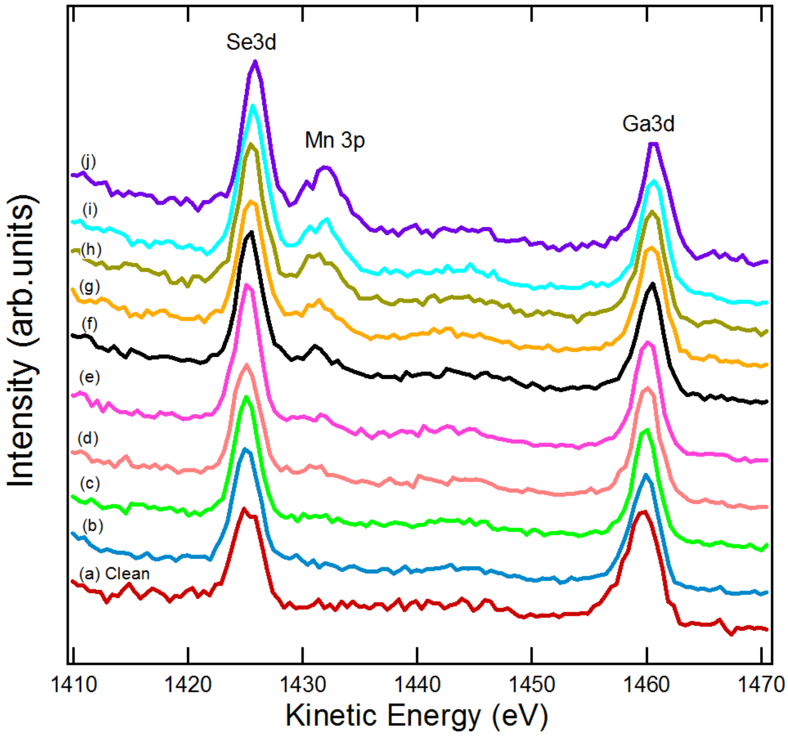

Figure 5.7: Spectra of Se3d, Mn3p and Ga3d shallow core levels collected from a clean ϵ-GaSe(0001) surface(a) and from a series of successively Mn-doped on ϵ-GaSe(0001) surface with constant flux rate at room temperature for 20 sec(b),40 sec(c), 60 sec(d), 80 sec(e), 100 sec(f), 120 sec(g), 140 sec(h), 160 sec(i), 180 sec(j) respectively .

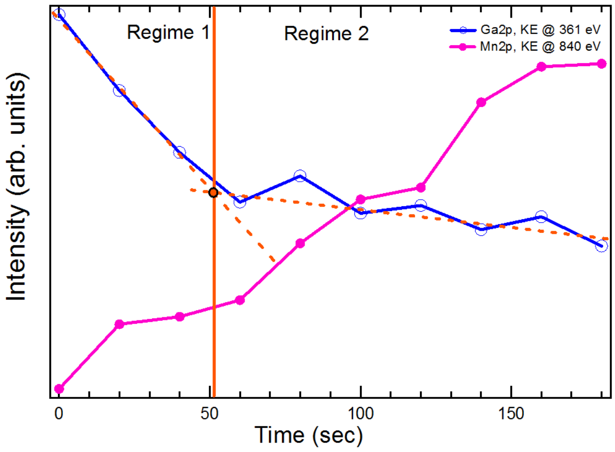

Figure 5.8: Intensities of Mn2p and Ga2p spectra for steps of Mn evaporated on ϵ-GaSe surface.

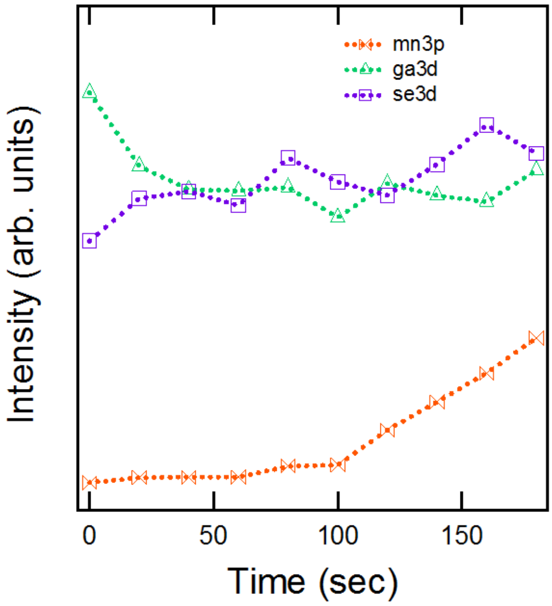

Figure 5.9: Intensities of Ga3d, Se3d and Mn3p spectra for steps of Mn evaporation on ϵ-GaSe surface.

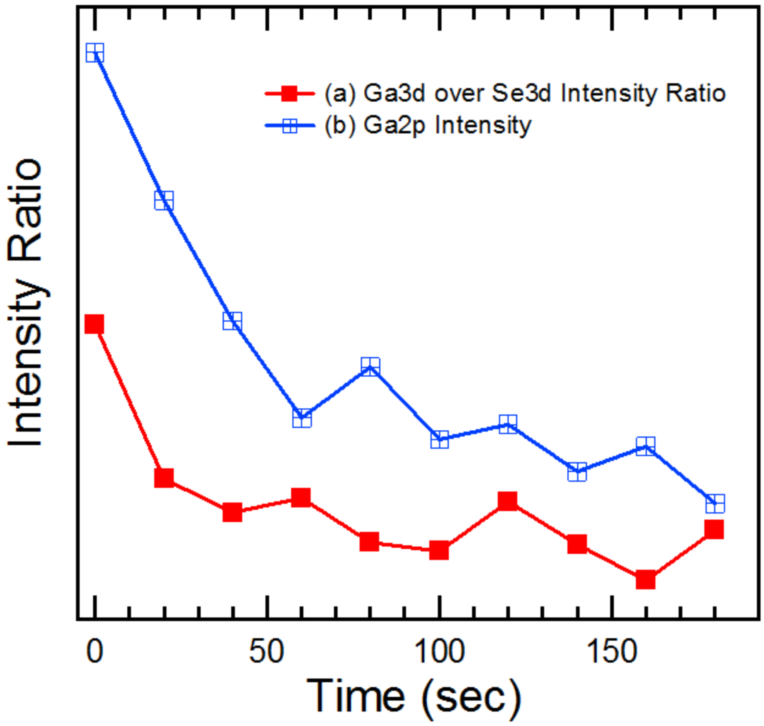

Figure 5.10: Intensity ratio between Ga3*d* and Se3*d* spectra (a), Intensities of Ga2*p* spectra(b), for steps of Mn evaporation on ϵ-GaSe surface.

detectable. The low kinetic energy of the Ga 2p electrons makes the spectra more sensitive to the surface layers. The decrease in the intensities of the Ga2*p* along with the increase of Mn2*p* intensity with respect to Mn deposition gives an indication of Mn substitution by Ga atom at the surfaces. It is important to note that the Ga 2p attenuation seems to follow two regimes. From 0 to about 50 seconds the attenuation is steeper than after 50 seconds. A similar behavior was found for Mn deposited on CdTe single crystals(98). As in that case, we can ascribe the steep decrease to Ga substitution with Mn, and the slower decrease with an overall screening of the Ga signal due to the growth of a segregated Mn overlayer. Therefore, after a determined Mn coverage, Mn diffusion through the surface and Ga substitution processed are hindered, resulting in the build up of Mn clusters or overlayers on the surface (Fig. 5.5).

This finding is consistent with the behavior detected for Ga and Se shallow core levels (Figure 5.9). Actually, the high kinetic energy of photoelectrons from Ga3*d* and Se3*d* make the probe more bulk sensitive, and a clear signal attenuation is not detected. This is ascribed to the larger bulk sensitivity which also probes layers well below the reacted surface and therefore negligibly affected by Ga substitution with Mn. However, if the intensity of Ga 3d is normalized over that of Se 3d, as shown in Fig.5.10, a steeper attenuation of Ga with respect to Se is again observed, as is evident from a comparison with the Ga 2p attenuation.

5.3 Annealed $Ga_{1-x}Mn_xSe$ Interface

A new sample of Mn doped on ϵ-GaSe(0001) surface has been prepared through Mn evaporation followed by annealing at 400 C. Annealing is meant to trigger the Mn diffusion, avoiding as much as possible the segregation of metallic Mn at the surface.

The electronic and magnetic properties of the system are studied by XPS, parameterized CI model calculations, XAS, ResPES and SQUID magnetic measurements in 5^o-300^o K range.

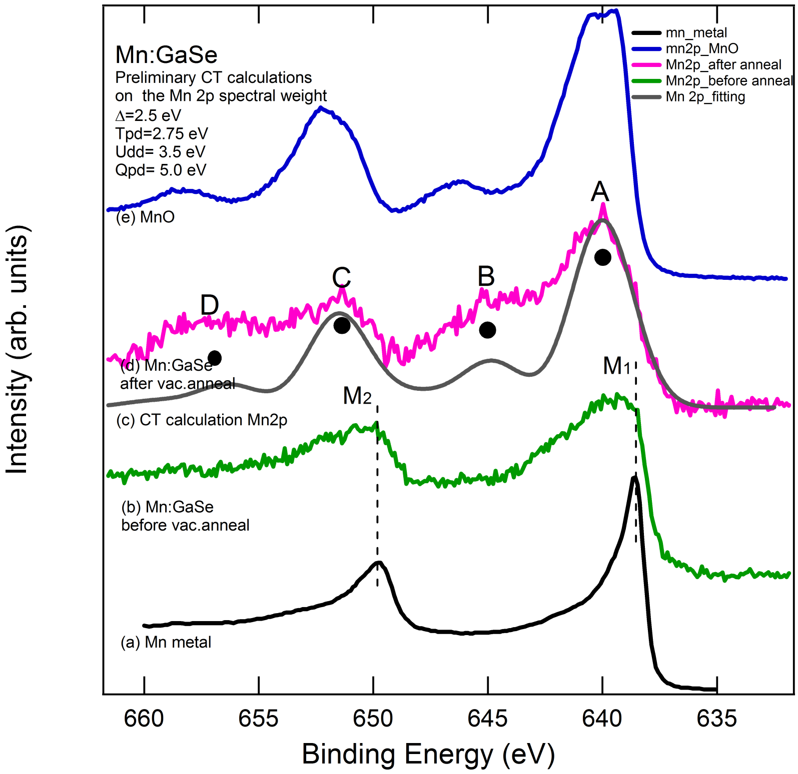

Figure 5.11: XPS spectra of the Mn 2p core lines collected from (a) a thick Mn metallic film, (b) the Mn:GaSe interface before UHV annealing, (c) CT calculations on the Mn 2p spectral weight,(d) Mn:GaSe interface after UHV annealing (e) a MnO single crystal

5.3.1 Core level XPS and parameterized CI calculations

Figure 5.11 shows the Mn 2p core line of the Mn:GaSe interface prior and after annealing in vacuum. As observed, the four spectral features of the vacuum annealed interface present strong satellites (B and D) on the high BE side of the main lines (A and C) of the Mn 2p spin-orbit split components. These features are reminiscent of the behavior on Mn in other DMS such as ZnS and CdTe$^{(95)}$. When properly analyzed, they can provide useful indications on the possible ligand-metal (i.e. Se-Mn) charge transfer effects.

We can exclude the presence of relevant oxygen contaminations, as the measured Mn 2p XPS lineshape is quite different from that of MnO (Figure 5.11-e). Furthermore, we did not observe any signal from oxygen within the sensitivity of our probe. The spectrum of the as-deposited film (Figure5.11-b) shows a manifold of features, ascribed to both metallic Mn and Mn diluted in the GaSe lattice. In fact, a comparison with the Mn 2p XPS core line from metallic Mn (Figure5.11-a) indicates that the M1 and M2 features (marked by dashed vertical lines) can be ascribed to metallic Mn. These features are progressively quenched with annealing treatments (Figure5.11-d), indicating that the annealing induces a substitution of Ga by Mn atom , rather than a clustering of Mn on the GaSe(0001) surface. The spectrum (5.11-c) can be described by four broad peaks (A,B,C and D). The peak A and C separated by the spin-orbit interaction and the width of these two peak is ascribed to disorder effects, related to replacement of Ga atom by Mn. On the high BE side of these peaks, two satellites are also detectable (B and D), quite similar to those found in Mn-based DMS, such as $Cd_{1-x}Mn_xTe$,$Zn_{1-x}Mn_xS$ and $Ga_{1-x}Mn_xAs$(95,86). They are ascribed to charge transfer effects from the ligand anions (Te, S or As, respectively) to the 3d levels of Mn cations. These effects can be accounted for in the frame of a configuration interaction model where the electronic states involved in the photoemission process are described by a linear combination of several configurations (see, e.g. Ref(86) and Refs. therein) such as $3d^n$, $3d^{n+1}L$, $3d^{n+2}L^2$,where L represents a hole in the ligand created by the charge transfer. The ligand-to-3d charge-transfer energy is defined by Δ=E(d^{n+1})-E(d^n). The intensity of B and D satellites varies depending on the charge transfer energy Δ, as well as on the hybridization strength (T) between the p and d orbitals involved in the charge transfer process (here from Se 4*p* to Mn 3*d*). Therefore, the line-shape analysis of the Mn 2p core levels shown in figure 5.11-d provides an evidence of Mn-Se hybridization effects for the Mn:GaSe system. A calculation of the Mn 2p spectral weight for a Mn^{2+} impurity in GaSe surface is shown in figure5.11-c. The calculated curve (Figure 5.11-c) has been obtained by setting Δ=2.5 eV, the on-site Coulomb repulsion $Udd = 3.5$ eV, Tpd=2.75 eV and the Mn 2p-3d coulomb interaction $Qpd = 5.0$ eV. These findings are consistent with those obtained on Mn-doped DMS(95,86). The charge transfer energy is rather high as compared to other DMS systems, as it roughly scales with the energy gap of the host crystal, that for GaSe is larger than for CdTe and GaAs.

5.4 Synchrotron Radiation measurements of $Ga_{1-x}Mn_xSe$ Interface

$Ga_{1-x}Mn_xSe$ samples have been prepared as described in the previous Section. In the following, further insight into the Mn:GaSe interface is achieved by resorting to XAS and ResPES experiments on annealed Mn:GaSe interfaces. The experimental data have been interpreted by referring to DFT calculations (valence band of undoped GaSe), and developing a CI model for the Mn 3d spectral weight in the valence band of $Ga_{1-x}Mn_xSe$. Finally, the XAS spectrum has been discussed at the light of atomic calculations for the Mn 2p-3d absorption process. The experiments have been carried out at the BACH beamline of the Elettra synchrotron in Trieste.

5.4.1 XAS

The Mn L-edge XAS spectra are shown in Figure 5.12, where the data obtained after the Mn deposition (f) and after annealing at 400^{o}C and collected at RT (e) and at 90 K (d) are presented. The as-deposited Mn-doped Mn:GaSe before annealing shows the presence mixed of both metallic and reacted Mn-GaSe interface. After annealing at 400^{o}C, sharper features (labeled as A, B, C, D, and E) appear, and the comparison with multiplet calculations for a Mn^{2+} $2p^6 3d^5 \rightarrow 2p^5 3d^6$ electric-dipole allowed transition unambiguously shows that the measured spectrum can be ascribed to a Mn^{2+} ion in the GaSe matrix. Similar transition calculated for Mn^{1+} (b) and Mn^{3+} (a) ions do not fit the experimental data.

The remarkable similarity with the XAS spectrum predicted for the Mn^{2+} calculation is particularly helpful for the interpretation of the electron spectroscopy results. As first, this justifies the assumption at the basis of CI calculations for the Mn 2p XPS data (see previous section) where an Mn^{2+} ion has been assumed as the ionic configuration in the parameterized charge transfer model. The same assumption, i.e. a Mn $^{2+}$, $3d^5$ ionic configuration, will also be at the basis of the charge transfer CI calculations for the Mn 3d spectral weight in the valence band. Mn L-edge XAS of annealed Mn doped GaSe films closely resembles result expected for atomic Mn in the +2 ($3d^5$) oxidation state which accounts for the bulk electronic properties of Mn in the annealed Mn:GaSe sample. From the right panel of figure 5.12, we have shown a series of calculated Mn XAS spectra starting from zero crystal field effect to 2.5 eV. It is also important to note that crystal field effects seem to be rather limited, as shown in Fig 5.13, where the experimental data are compared to the spectrum calculated by introducing a tetrahedral T_d crystal field with 10Dq=0.75 eV. i.e. the crystal field value where two spectral features distinctively appear on the low photon energy side of each threshold, making the calculated spectrum distinguishable from the zero crystal field case. Already at this value, the two features appearing on the low photon energy sides of both MnL_{III} and MnL_{II} calculated peaks that have no counterpart in the experimental data. Therefore, we assume that crystal field effects can be negligible. This remark will also be at the basis of the CI model for the valence band calculations, where crystal field splitting will be set to zero.

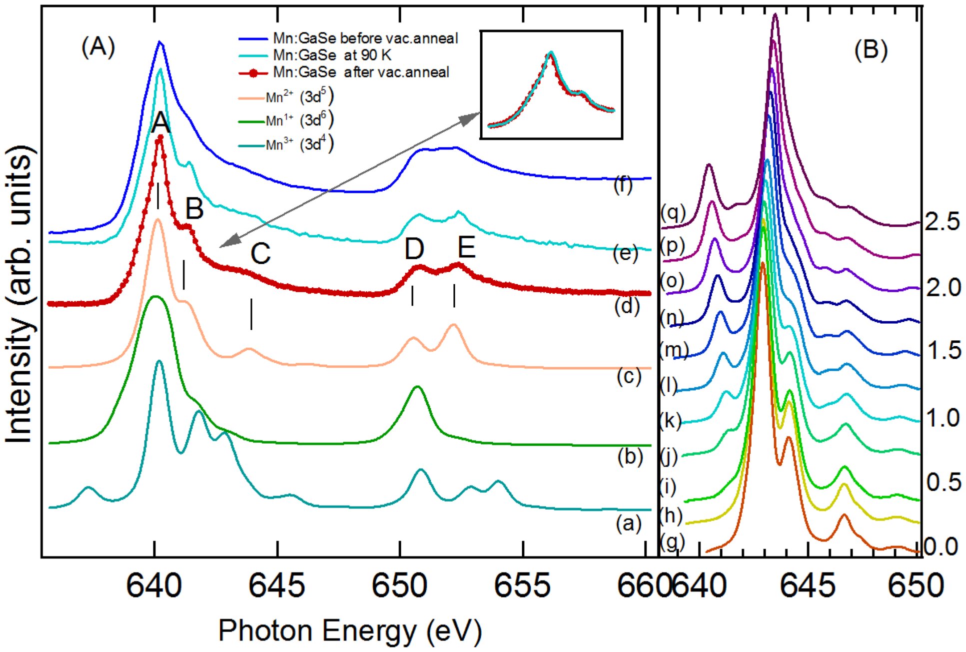

Figure 5.12: The left figure (A) shows Experimental Mn L-edge XAS spectra of Mn deposited on GaSe surface with out annealing figure (f), after annealing figure (d) and after cooling the annealed surface at around 90 K figure (e). It has also been compared with computed result for atomic Mn L-edge XAS spectra for the +3 oxidation state ($3d^4$) in figure(a), +1 oxidation state($3d^6$) in figure (b),+2 oxidation state ($3d^5$) in figure(c) with zero crystal field. Mn L-edge XAS of annealed Mn doped GaSe films closely resembles the result expected for atomic Mn in the +2 (3d5) oxidation state which accounts for the bulk electronic properties of Mn in the annealed Mn:GaSe sample. The right figure (B) shows a series of calculated XAS spectrum with different crystal field starting from 0 to higher values.

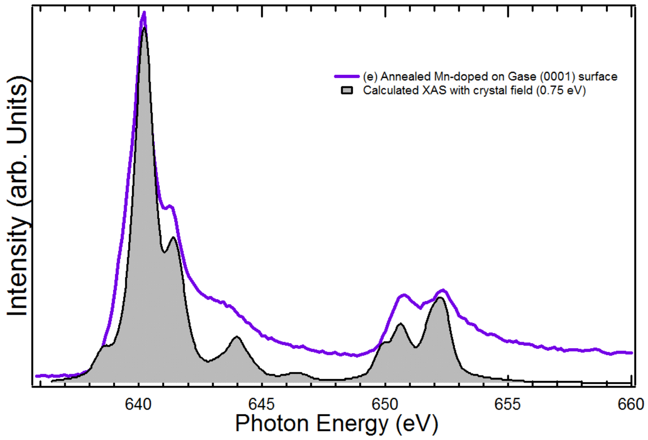

Figure 5.13: Comparison between the experimental XAS spectrum of the annealed Mn:GaSe interface and the calculated XAS spectrum for the atomic Mn^{2+} 3d5 configuration with a tetrahedral crystal field splitting of 0.75 eV.

5.4.2 Valence Band Photoelectron spectroscopy

The valence band spectra of the pure undoped GaSe and of the Mn-doped, annealed, GaSe single crystals are shown in Figure 5.14 (b) and (a), respectively. The photoemission spectra have been collected with a photon energy of 797 eV and have been normalized to the maximum of the valence band emission (peak A). Both spectra show a main line with three features labeled A', A, and B, and a peak C at higher binding energies. When Mn is evaporated on the GaSe cleaved surface, the main changes that can be observed are the appearance of a feature A" at the Fermi edge, and an increase of the spectral weight in the regions between the peaks A and B and the peaks B and C. The curve displayed in Fig 5.14 (c) represents the difference between the spectra (a) and (b). This difference confirms the increase of spectral weight in the 3-7 eV binding energy range, and in the region just below the Fermi edge(BE=0-2 eV), while a decrease of the intensity is found below peak C after Mn deposition and annealing at 400^o C.

The calculated DOS in the valence band is shown in 5.14 (d). As can be observed, the calculation reproduces the main features of the valence band emission, though they appear to be slightly shrunk in a binding energy range of about 7 eV, while the experimental data span an energy range of about 8 eV. The empty states appear close to 0 eV as an effect of shrinking in the calculation DOS. The projected DOS are shown in Fig. 5.14(e) (Se s, p

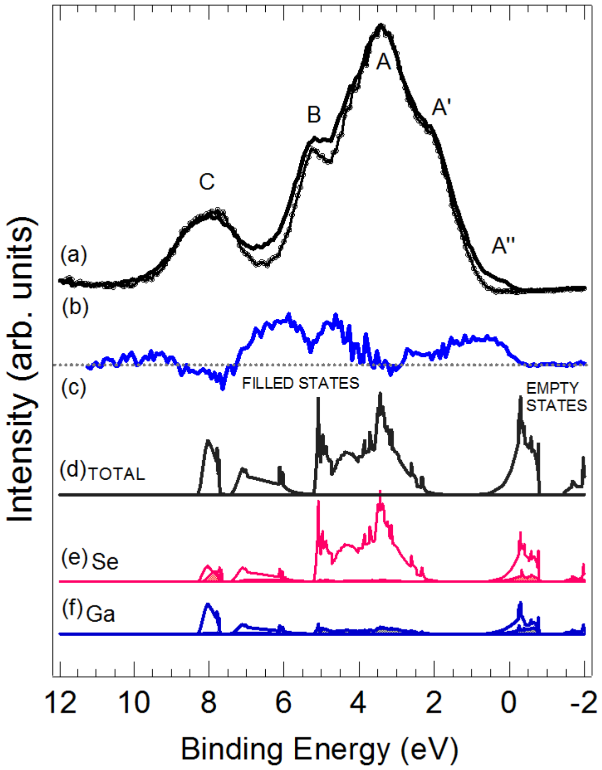

Figure 5.14: Valence band spectra of the clean GaSe (b) and of the Mn-doped, annealed, GaSe single crystal (a). Difference between the spectra of the doped and the clean system (c). Total DOS calculated with the ABINIT code (d). Selenium s and p projected density of states (e), Gallium s and p projected density of states (f).

states) and fig. 5.14(f) (Ga s, p states). It is rather interesting to observe that the electronic states of the Ga cation mainly contributes in the region below peak C, i.e. in the region where a minor spectral weight decrease is detectable upon Mn doping and annealing. This is in agreement with a process of Ga substitution with Mn atoms, as remarked at the beginning of this Chapter. Finally, the states appearing at the Fermi edge can be ascribed to some unreacted metallic Mn at the surface.

5.4.3 Resonant photoelectron spectroscopy at the Mn 2p-3d absorption edge

In order to enhance the Mn contribution to valence band states, a ResPES study at the Mn 2p-3d absorption edge has been carried out. The results are shown in Fig 5.15. As first, on the XAS spectrum(A) the photon energies(spectrum a to j) selected to collect ResPES data are indicated. The whole set of ResPES data is shown in panel (B). The data span a photon range across the Mn L_{III} threshold. The VB spectra show a clear enhancement of the spectral weight with a photon energy of about 640.1 eV. At this energy a peak around BE= 4eV in the valence band shows a remarkable intensity enhancement. The difference between the resonant and off-resonance spectra is shown in panel C. Here it is clearly seen that the resonating spectral weight (RSW) is determined by a peak at 4 eV and by two peaks at about BE= 7 eV and BE= 1 eV.

The origin of the three peaks in the RSW can be discussed at the light of parameterized CI calculations for the valence band. The calculations have been carried out following the scheme presented by Fujimori et al.(97) for several Mn doped semiconductors, based on a $3d^5$ initial state of the transition metal atom(94). The results are shown in Fig. 5.16, along with those obtained on a Mn-doped CdTe single crystal(95,96). The peaks observed at the resonance are labeled as R1, R2, and R3. The parameter set used in the calculation is reported in Table Fig. 5.17.

The comparison with the RSW detected under the same conditions for the Mn-doped CdTe crystal is rather interesting. The gray spectrum in the top panel represents the resonance spectrum collected from an heavily doped CdTe single crystal. It is shown here to point out the contribution at the Fermi level of metallic Mn segregations, which well compare, with the states observed in the GaSe host crystal, though these states are less intense in the latter system. Also in the CdTe case, three peaks appear in the resonant spectrum, but the relative weight and width of these peaks are different from the Mn:GaSe case. Peak R2 is larger in the GaSe host, and the separation between peak R1 and R2 is larger in the GaSe host with respect to the CdTe case. These differences have been considered as constraints in the calculations. In particular, the calculations for the GaSe case have been obtained by setting the crystal field to zero and by considering a large charge transfer energy as compared to CdTe (Fig. 5.17). The first assumption is

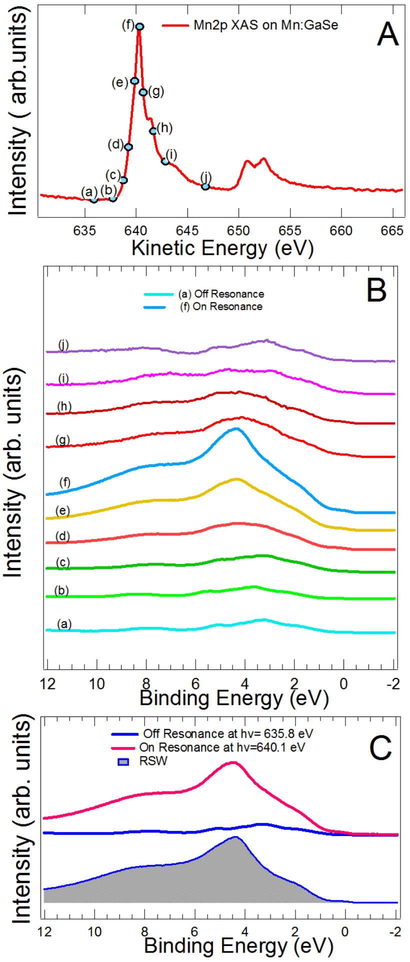

Figure 5.15: (A) XAS spectrum of the Mn-GaSe interface collected at the Mn 2p-3d edge. The dots indicate the photon energies chosen to collect the, resonant, valence band photoemission spectra. (B) Set of valence band spectra collected at different photon energies across the Mn 2p-3d edge. (C) Off-resonance and resonant VB spectra collected at 635.8 eV and 640.1 eV, respectively. Difference between the resonant and off-resonance spectra (shaded area).

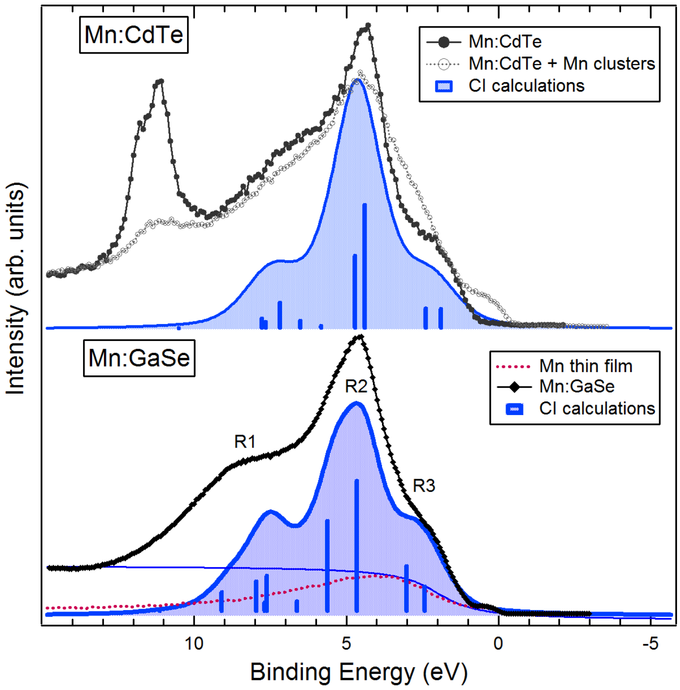

Figure 5.16: Experimental data and CI calculations for the Mn:CdTe (top panel) and the Mn:GaSe (bottom panel) interfaces. The shaded areas represent the CI calculations, while the vertical bars indicate the eigenenergies obtained by solving the Hamiltonian matrix (see Chapt. 2.6). The height of each bar is proportional to the square of the projection of the eigenvector on the ground, initial, state. All energies are given in eV.

justified by the lack of relevant crystal field effects observed in XAS, whereas the second, in agreement with what already found in core levels Mn 2p XPS, is justified by the larger band gap of GaSe with respect to CdTe. This choice of the parameter set resulted in a broadening of the peak below R2, as an effect of CF=0, and in the intensity increase and BE shift of calculated spectral weight below R1. Also the calculated spectral weight below R3 is increased, in agreement with the measured data.

We used the free ion Racah parameter for Mn^{2+}, B=0.126, C=0.421, and the crystal field was set at 0.4 eV for the CdTe host and 0 eV for the GaSe host.

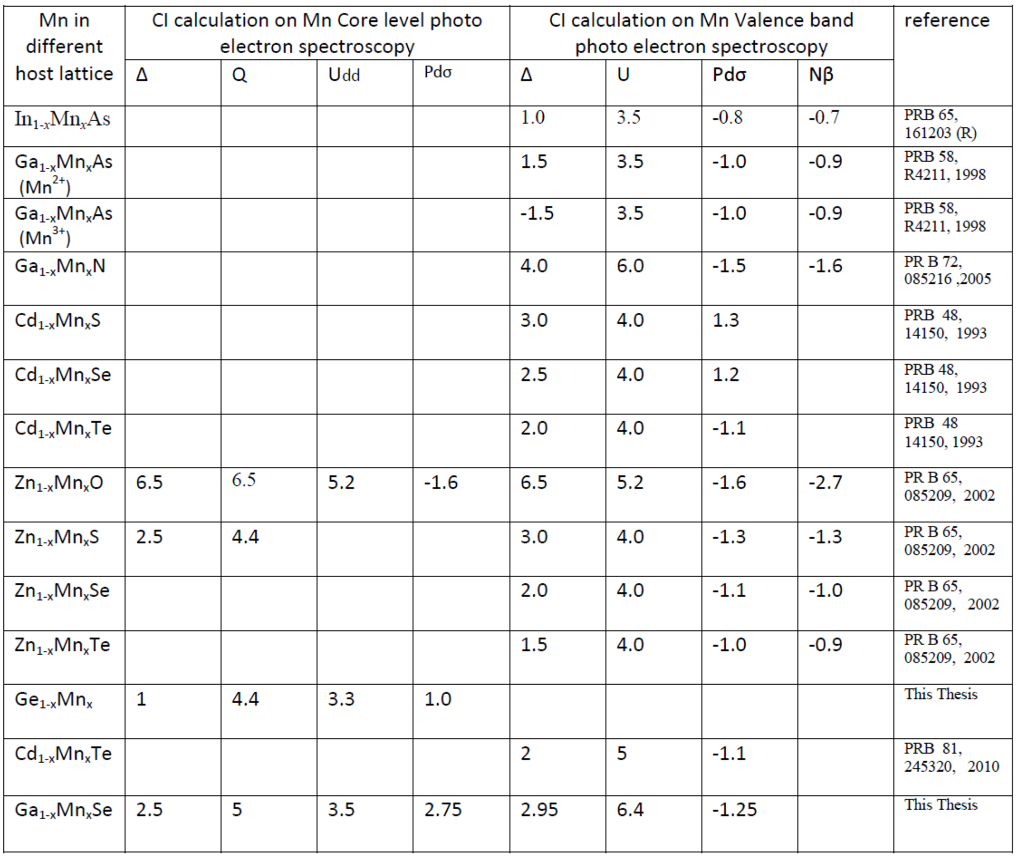

Mn in different host lattice	CI calculation on Mn Core level photo electron spectroscopy				CI calculation on Mn Valence band photo electron spectroscopy				reference
	Δ	Q	Udd	Pdσ	Δ	U	Pdσ	Nβ	
$In_{1-x}Mn_xAs$					1.0	3.5	-0.8	-0.7	PRB 65, 161203 (R)
$Ga_{1-x}Mn_xAs$ (Mn^{2+})					1.5	3.5	-1.0	-0.9	PRB 58, R4211, 1998
$Ga_{1-x}Mn_xAs$ (Mn^{3+})					-1.5	3.5	-1.0	-0.9	PRB 58, R4211, 1998
$Ga_{1-x}Mn_xN$					4.0	6.0	-1.5	-1.6	PR B 72, 085216 ,2005
$Cd_{1-x}Mn_xS$					3.0	4.0	1.3		PRB 48, 14150, 1993
$Cd_{1-x}Mn_xSe$					2.5	4.0	1.2		PRB 48, 14150, 1993
$Cd_{1-x}Mn_xTe$					2.0	4.0	-1.1		PRB 48 14150, 1993
$Zn_{1-x}Mn_xO$	6.5	6.5	5.2	-1.6	6.5	5.2	-1.6	-2.7	PR B 65, 085209, 2002
$Zn_{1-x}Mn_xS$	2.5	4.4			3.0	4.0	-1.3	-1.3	PR B 65, 085209, 2002
$Zn_{1-x}Mn_xSe$					2.0	4.0	-1.1	-1.0	PR B 65, 085209, 2002
$Zn_{1-x}Mn_xTe$					1.5	4.0	-1.0	-0.9	PR B 65, 085209, 2002
$Ge_{1-x}Mn_x$	1	4.4	3.3	1.0					This Thesis
$Cd_{1-x}Mn_xTe$					2	5	-1.1		PRB 81, 245320, 2010
$Ga_{1-x}Mn_xSe$	2.5	5	3.5	2.75	2.95	6.4	-1.25		This Thesis

Figure 5.17: Parameter values used for the parameterized CI calculation of the Mn 3d spectral weight in valence and core level photo electron spectroscopy for semiconductors. The followings are specified: the pdσ hybridization integral, the charge transfer energy Δ, the correlation energy U of the $3d^{n+2}\underline{L}^2$ configurations, core-hole 3d electron Coulomb attraction Q_{pd}.

5.4.4 Magnetic Measurements

Magnetic measurements have been carried out with a SQUID magnetometer at the university of Pavia in a 5^o-300^o K range in fields of 0.01 and 0.5 T.

The M vs. T data collected at 100 and 5000 Gauss are shown in the Figure 5.18, where magnetization increases with temperature under low (100 Gauss) and high (5000 Gauss) external fields, with a sharp transition at 150 K. This transition becomes less sharp as the external field is increased from 100 to 5000 Gauss. The behavior in magnetic measurement is similar to that observed for $Ga_{1-x}Mn_xSe$ single crystals(81), though differences have to be pointed out. Also for Mn-doped single crystals a jump in magnetization is observed at about 115 K(Fig. 5.19), while in our case the jump is detected at higher temperatures (150 K). Furthermore, we do not observe a quenching of magnetization up to 320 K, i.e. the upper limit of our probe, while in Mn-doped single crystals a quenching of magnetization is observed at about 190 K. Though in both cases the jump is quenched at higher external fields, the quenching is larger for the Mn-doped single crystals than in the present case.

As compared to magnetization in possible segregated phases, we observe that the magnetization behavior of related compounds such as Mn-Se bulk phases(88) or and $MnGa_2Se_4$(89) is quite different from the present magnetic data.

(i) The magnetic susceptibility in MnSe and $MnSe_2$ is known to obey the Curie-Weiss law in the temperature range 120-300 K for α-MnSe and 50-300 K for $MnSe_2$, due to a considerably strong anti-ferromagnetic interaction between adjacent Mn^{2+} ions through Se^{2-} bridges. The magnetic susceptibility of our sample increases with temperature up to 300 K, which contradicts the magnetic susceptibility χ behavior observed in α-MnSe and $MnSe_2$ in the temperature range of 50-300 K .

(ii) Looking at the behavior of the inverse susceptibility $(1/\chi)$ with temperature of our annealed Mn-doped GaSe sample (inset Fig. (C) 5.18) and a bulk $MnGa_2Se_4$ (Fig.1 of ref(89)), we rule out the presence of a major contribution from $MnGa_2Se_4$ segregated phase, Indeed, while $MnGa_2Se_4$ shows an anti-ferromagnetic behavior with Neel temperature at 8 K(89) with a linear increase of $1/\chi$ with temperature. Where as, our sample shows a decrease of $1/\chi$ with temperature. Other Mn-Se bulk phases show an antiferromagnetic

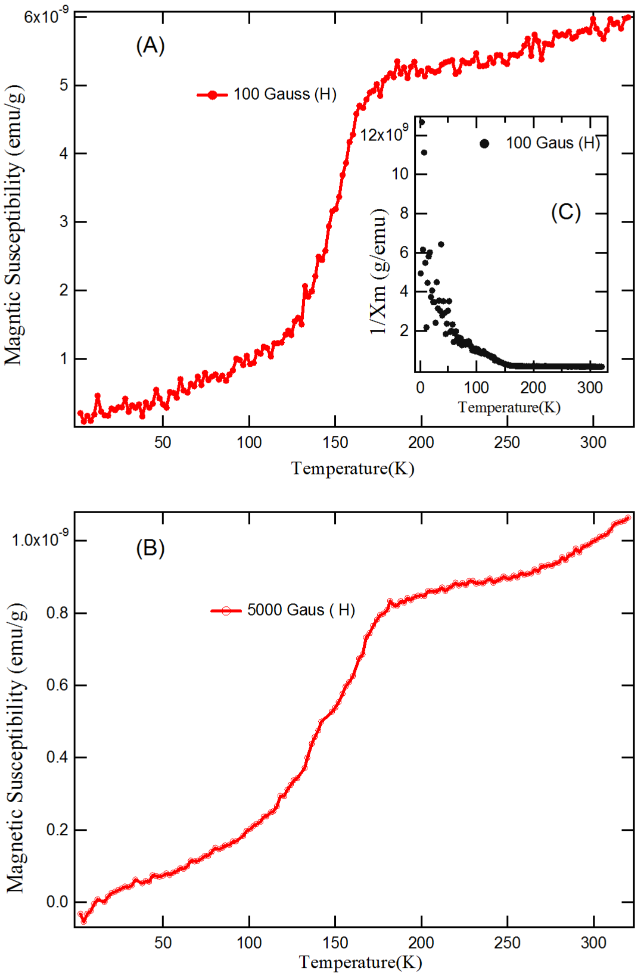

Figure 5.18: Magnetic Susceptibility χ vs Temperature(T) curves of the Ga$_{1-x}$Mn$_x$Se surface alloys obtained at 100 Gauss(A), 5000 Gauss(B) and $1/\chi$ vs Temperature (T) curve obtained at 100 Gauss(C).

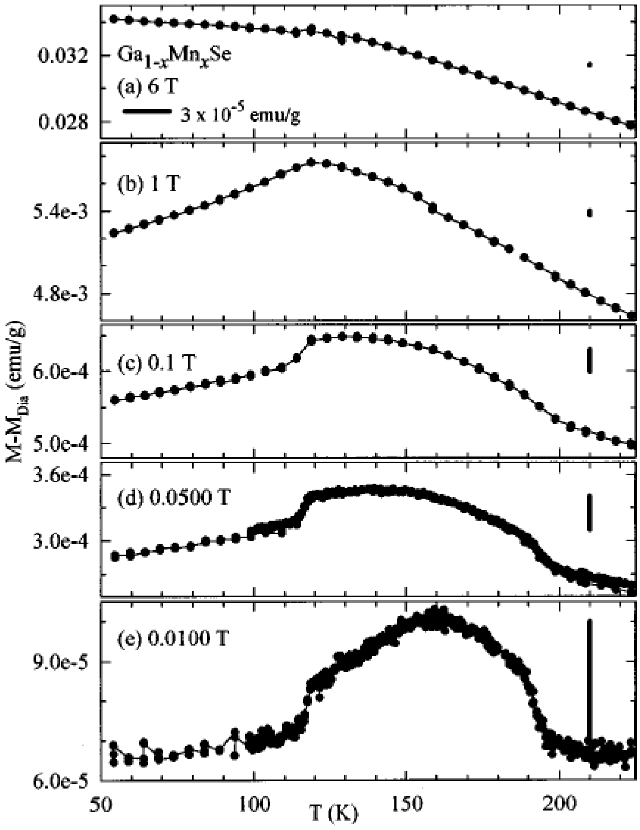

Figure 5.19: M vs T curves of the Ga$_{1-x}$Mn$_x$Se single crystal as reported in the paper Pekarek et. al.$^{(81)}$.

behavior with different structural changes with respect to temperature(99).

The behavior we observe in magnetic measurement looks similar to that of a system displaying spin-crossover as the temperature is changed(87). Alternatively, the behavior can be ascribed to a strong temperature dependence of the carrier-mediated ferromagnetism similarly observed in Mn:InSb alloy(87). To check the first hypothesis, we reconsider the XAS measurements carried out at low T, in order to track possible changes in the local electronic properties of Mn ions driven by structural effects. Indeed, a structural change may lead to a different crystal field splitting that could be related to a low-spin to high-spin transition in the metallic cation. The high-T and low-T Mn^{2+} XAS spectra are virtually identical, ruling out, within the experimental sensitivity of the probe, changes in the local environment as a source of low-spin to high-spin transitions. The second scenario deserves further investigations, starting from the search of hysteresis loops that were not investigated in this set of magnetization studies.

5.5 Conclusion

We have been able to prepare well characterized Mn:GaSe interfaces, with evidence of the formation of a $Ga_{1-x}Mn_xSe$ surface alloy. Our measurements on the electronic properties of this system have shown the capability of Mn to diffuse into the lattice with a remarkable hybridizations with Se anions. A magnetic behavior that apparently could be related to some robust single crystal of $Ga_{1-x}Mn_xSe$ and a spin-crossover transition has been observed, but temperature dependent XAS measurements rule out possible high-spin to low-spin transitions on the basis of an analysis of multiplet fine structure appearing at the Mn 2p-3d absorption threshold. Rather, an RKKY mechanism could be invoked to explain the increase of M with T, supported by the creation of free carriers as the temperature is increased. Therefore, it is likely that the peculiar magnetic behavior we observe can be ascribed to the top-most surface layers and rationalized in the frame of surface or interface magnetization, rather than bulk magnetism.

Bibliography

[1] G Prinz 1995 Phys. Today **48(4)** 58

[2] T Dietl, H. Ohno and F. Matsukura 2001 Phys. Rev B **63** 195205

[3] H Ohno 1998 SCIENCE **281**(5379) 951-956

[4] E Arras, D Caliste, T Deutsch, F Lançon, and P Pochet, 2011 Phys. Rev B **83** 174103

[5] Xiu F, Wang Y, Kim J, Upadhyaya P, Zhou Y, Kou X, Han W, Kawakami R, Zou J and Wang K, 2010 ACS Nano **4** 4948

[6] Park Y D, Hanbick AT, Erwin SC, Hellberg CS, Sullivan JM, Mattson JE, Ambrose TF, Wilson A, Spanos G, Jonker BT 2002 Science **295** 651

[7] Jamet M, Barski A, Devillers T, Poydenot V, Dujardin R, Bayle-Guillemaud P, Rothman J, Bellet-Amalric E, Marty A, Cibert J, Mattana R, Tatarenko S 2006 Nature Materials **5** 653

[8] T Devillers, M Jamet, A Barski, V Poydenot, P Bayle-Guillemaud, and E Bellet-Amalric, S Cherifi and J Cibert 2007 Phys. Rev. B **76** 205306

[9] A P Li, J F Wendelken, and J Shen, L C Feldman, J R Thompson and H H Weitering, 2005 Phys. Rev B **72** 195205

[10] Zeng C, Erwin S C, Feldman L C, Li A P, Jin R, Song Y, Thomson J R and Weitering H H 2003 Appl. Phys. Lett. **83** 5002

[11] C Zeng, W Zhu, S C Erwin, Z Zhang and H H Weitering 2004 Phys. Rev. B **70** 205340

[12] Sangaletti L, Ghidoni D, Pagliara S, Goldoni A, Morgante A, Floreano L, Cossaro A, Mozzati MC, Azzoni CB 2005 Phys. Rev. B **72**, 35434

[13] S Guchhait, M Jamil, H Ohldag, A Mehta, E Arenholz, G Lian, A LiFatou, D A Ferrer, J T Markert, L Colombo, and S K Banerjee 2011 Phys. Rev. B **84** 024432

[14] Y D Park, A Wilson, A T Hanbicki, J E Mattson, Ambrose, G Spanos and B T Jonker 2001 Appl. Phys. Lett. **78** 2739

[15] Mustafa M Özer, James R Thompson and H H Weitering 2012 Phys. Rev. B **85** 125208

[16] C Zeng, Z Zhang, K van Benthem, M F Chisholm and H H Weitering 2008 Phys. Rev. Lett. **100** 066101

[17] Brühwiler P A, Karis O, Martensson N 2002 Rev. Mod. Phys. **74** 703

[18] Föhlisch A, Menzel D, Feulner P, Ecker M, Weimar R, Kostov K L, Tyuliev G, Lizzit S, Larciprete R, Hennies F, Wurth W 2003 Chemical Physics **289** 107

[19] Vilmercati P, Cvetko D, Cossaro A, Morgante A 2009 Surf. Sci. **603** 1542

[20] Mentes T O, Bondino F, Magnano E, Zangrando M, Kuepper K, Galakhov V R, Mukovskii Y M, Neumann M and Parmigiani F 2006 Phys. Rev. B **74** 205409

[21] Richter M C, Bencok P, Brochier R, Ilakovac V, Heckmann O, Paolucci G, Goldoni A, Larciprete R, Gallet J-J, Chevrier F, Van der Laan G, Hricovini K 2001 Phys. Rev B **63** 205416

[22] Richter M C, Mariot J -M, Heckmann O, Kjeldgaard L, Mun B S, Fadley C S, Hricovini K 2006 Nuclear Instruments and Methods in Physics Research B **246** 184

[23] Taguchi Y, Kitamoto K, Mimura K, Kawamata S, Ishida T, Aita O, Ichikawa K 2007 Journal of Electron Spectroscopy and Related Phenomena **156-158** 430

[24] Fujiwara H, Sekiyama A, Yano M, Murakawa T, Miyamachi T, Tsunekawa M, Imada S, Schmid B, Sing M, Higashiya A, Muro T, Nakamura T, Noda K, Kuwahara H, Miyasaka S, Tokura Y, Suga S 2007 Journal of Magnetism and Magnetic Materials **310** 816

[25] Hashimoto R, Chikamatsu A, Kumigashira H, Oshima M, Nakagawa N, Ohnishi T, Lippma M, Wadati H, Fujimori A, Ono K, Kawasaki M, Koinuma H 2005 Journal of Electron Spectroscopy and Related Phenomena **144-147** 479

[26] Eguchi R, Yoshid H, Okamoto Y, Chainani A, Matsunami M, Ishida Y, Oura M, Senba Y, Ohashi H, Shin S, Hiroi Z 2010 Journal of the Physical Society of Japan **79** 023704

[27] Reinert F, Steiner P, Blaha P, Claessen R, Zimmermann R, Hufner S 1995 Journal of Electron Spectroscopy and Related Phenomena **76** 671

[28] Kang J -S, Kim G, Lee H J, Kolesnik S, Dabrowski B, Lee H, Kim J -J, Lee J, Kim B, Min B I 2009 J. of Appl. Phys. **105** 07D721

[29] Takeuchi T, Nozaki H, Soda K, Kondo T, Mizutani U, Yokoya T, Sato T, Takahashi T, Shin S, Muro T, Saitoh Y, Moritomo Y 2002 J. Synchrotron Rad. **9** 237

[30] Biegger E, Stheli L, Fonin M, Rdiger U, Dedkov Y S 2007 J. of Appl. Phys. **101** 103912

[31] Adell J, Ulfat I, Sadowskic J, Ilver L, Kanski J, 2011 Solid State Communications **151** 850

[32] Sato H, Senba S, Okuda H, Nakateke M, Furuta A, Ueda Y, Taniguchi M, Tanaka A, Jo T 1998 Journal of Electron Spectroscopy and Related Phenomena **88-91** 425

[33] Yablonskikh M V, Shkvarin A S, Yarmoshenko Y M, Skorikov N A, Titov A N 2012 J. Phys.: Condens. Matter **24** 045504

[34] del Pennino U, De Renzi V, Biagi R, Corradini V, Zobbi L, Cornia A, Gatteschi D, Bondino F, Magnano E, Zangrando M, Zacchigna M, Lichtenstein A, Boukhvalov D W 2006 Surface Science **600** 4185

[35] Petraki F, Peisert H, Hoffmann P, Uihlein J, Knupfer M, Chasse T, 2012 J. Phys. Chem. C **116** 5121

[36] Horn K , Theis W, Paggel J J, Barman S R, Rotenberg E, Ebert Ph, Urban K 2006 J. Phys.: Condens. Matter **18** 435

[37] Yablonskikh M V, Shkvarin A S, Yarmoshenko Y M, Skorikov N A, Titov A N 2012 J. Phys.: Condens. Matter **24** 045504

[38] A. Verdini, A. Cossaro, L. Floreano, A. Morgante, A. Goldoni, D. Ghidoni, A. Sepe, S. Pagliara and L. Sangaletti 2008 Phys. Rev. B **77** 075405

[39] Sangaletti L, Pagliara S, Parmigiani F, Goldoni A, Floreano L, Morgante A, Aguekian V 2003 Phys. Rev. B **67** 233201

[40] Rader O, Pampuch C , Shikin A M, Gudat W, Okabayashi J, Mizokawa T, Fujimori A, Hayashi T, Tanaka M, Tanaka A, Kimura A 2004 Phys. Rev. B **69** 075202

[41] Davis L C, Feldkamp L A, 1977 Phys. Rev. B **15** 2961

[42] Hüfner S, Yang S-H, Mun BS, Fadley CS, Schafer J, Rotenberg E, Kevan SD 2000 Phys. Rev. B **61** 12582

[43] Kaurila T, Uhrberg R, Vayrynen J 1998 J. Electron Spectr. Relat. Phen. **88-91** 399

[44] Ilakovac V, Kralj M, Pervan P, Richter MC, Goldoni A, Larciprete R, Petaccia L, Hricovini K 2005 Phys. Rev. B **71** 085413

[45] Zangrando M, Magnano E, Nicolaou A, Carleschi E, Parmigiani F 2007 Phys. Rev. B **75** 233402

[46] Weinelt M, Nilsson A, Magnuson M, Wiell T, Wassdahl N, Karis O, Föhlisch A, Martensson N, Stöhr J, Samant M 1997 Phys. Rev. Lett. **78** 967

[47] Tjeng L H, Chen CT, Ghijsen J, Rudolf P, Sette F 1991 Phys. Rev. Lett. **67** 501

[48] Zutic I, Fabian J, Das Sarma S 2004 Rev. Mod. Phys. **76** 323

[49] Panguluri R P, Zeng C, Weitering H H, Sullivan J M, Erwin S C, Nadgorny B 2005 phys. stat. sol. (b) **242**, R67

[50] Floreano L, Naletto G, Cvetko D, Gotter R, Malvezzi M, Marassi L, Morgante A, Santaniello A, Verdini A, Tommasini F and Tondello G 1999 Rev. Sci. Instrum. **70** 3855

[51] Sangaletti L, Drera G, Magnano E, Bondino F, Cepek C, Sepe A and Goldoni A 2010, Phys. Rev. B **81** 085204

[52] Verdini A, Cossaro A, Floreano L, Morgante A, Goldoni A, Ghidoni D, Sepe A, Pagliara S and Sangaletti L 2008 Phys. Rev. B **77** 75405

[53] Pagliara S, Sangaletti L, Goldoni A, Kim C, Shen Z-X, Revcolevschi A, Dhalenne G, Parmigiani F 2002 Phys. Rev. B **65** 205107

[54] Wang L, Chen W, Thye Shen Wee A 2008 Surface Science Reports **63** 465

[55] Zeng C, Zhu W, Erwin C, Zhang Z, Weitering HH 2004 Phys. Rev. B **70** 205340

[56] Kim H, Jung G -E, Lim J -H, Chung K H, Kahng S -J, Som W -J, Han S 2008 Nanotech **19** 025707

[57] Forsyth J B, Brown P J 1990 J. Phys. Condens. Matter **2** 2713

[58] Hirvonen Grytzelius J, Zhang H M, Johansson L S O 2011 Phys. Rev. B **84** 195306

[59] Picozzi S, Continenza A, Freeman A J 2004, Phys. Rev. B **70** 235205

[60] A Verdini, A Cossaro, L Floreano, A Morgante, A Goldoni, D Ghidoni, A Sepe, S Pagliara, L Sangaletti Surface Science 2006 **600** 4369

[61] P S Bagus, J W Mallow 1994 Chem. Phys. Lett. **228** 695

[62] J Okabayashi, A Kimura, O Rader, T Mizokawa, A Fujimori, T Hayashi and M Tanaka, 1998 Phys. Rev. B **58** R4211

[63] G van der Laan, S S Dhesi, E Dudzik 2000 Phys. Rev. B **61** 12277

[64] F Carbone, M Zangrando, A Brinkman, A Nicolaou, F Bondino, E Magnano, A A Nugroho, F Parmigiani, Th Jarlborg and D van der Marel 2006 Phys. Rev. B **73** 085114

[65] P De Padova, J-P Ayoub, I Berbezier, P Perfetti, C Quaresima, A M Testa, D Fiorani, B Olivieri, J-M Mariot, A Taleb-Ibrahimi, M C Richter, O Heckmann and K Hricovini 2008 Phys. Rev. B **77** 045203

[66] Core Level Spectroscopy of Solids, Frank de Groot and Akio Kotani, CRC Press, Taylor and Francis Group

[67] R. C. Albers, J. J. Rehr., 2000 Rev. Mod. Phys. **72** 621

[68] P. W. Anderson, 1961 Phys.Rev. **124** 41

[69] F. D. M. Haldane and P. W. Anderson 1976 Phys. Rev. B **13** 2553

[70] M. lanoo and J. Bourgoin Point defects in semiconductors, Springer, Verlag, Berlin, 1981

[71] T.Mizokawa and A Fujimori 1997 Phys Rev B **56** 6669

[72] S. Sugano, Y. Tanabe and Y. Kaminura, Multiplets of Transition Metal Ions in Crystals, Academic Press, New York, 1970

[73] J.Kanamori 1963 Prog. Theor. Phys. **30** 275

[74] T.Mizokawa and A Fujimori 1993 Phys Rev B **48** 14150

[75] P A Brühwiler, O Karis and N Mårtennson 2002 Rev. Mod. Phys. **74** 703

[76] H Agren and F Gelmukhanov 2000 J. Electron Spectrosc. Relat. Phenom. **110-111** 153-178

[77] F Gelmukhanov and H Agren 1999 Phys. Rep. **312** 87

[78] N Mårtennson, M Weinelt, O Karis, M Magnuson, N Wassdahl, A Nilsson, J Stohr and M Samant 1997 Appl. Phys A **65** 159

[79] O Karis, A Nilsson, M Weinelt, T Wiell, C Puglia, N Wassdahl, N Mårtensson, M Samant and J Stohr 1996 Phys. Rev. Lett. **76** 1380

[80] U Fano 1961 Phys. Rev. **124** 1866

[81] T M Pekarek, B C Crooker, I Miotkowski and A K Ramdas 1998 Journal of Applied Physics **83** 6557

[82] T C Lovejoy, E N Yitamben, S M Heald, F S Ohuchi and M A Olmstead, Applied Physics Letters 2009 **95** 241907

[83] L Plucinski and R L Johnson, B J Kowalski, K Kopalko and B A Orlowski, Z D Kovalyuk and G V Lashkarev 2003 Phys. Rev. B **68** 125304

[84] Taisuke Ohta, D A Schmidt, Shuang Meng, A Klust, A Bostwick, Q Yu, Marjorie A Olmstead and F S Ohuchi 2005 Phys. Rev. Lett. **94** 116102

[85] T C Lovejoy, E N Yitamben, S M Heald, F S Ohuchi and M A Olmstead 2011 Phys. Rev. B **83** 155312

[86] Okabayashi J, Kimura A, Rader O, Mizokawa T, Fujimori A, Hayashi T and Tanaka M, 1998 Phys. Rev. B **58** R4211

[87] V N Krivoruchko, V Yu Tarenkov, D V Varyukhin, A I D'yachenko, O N Pashkova, V A Ivanov 2010 Journal of Magnetism and Magnetic Materials **322** 915-923

[88] Qing Peng, Yajie Dong, Zhaoxiang Deng, Huizhong Kou, Song Gao and Yadong Li 2002 J. Phys. Chem. B **106** 9261-9265

[89] M Morocoima, M Quintero, E Quintero, J Gonzlez, R Tovar, P Bocaranda, J Ruiz, N Marchn, D Caldera and E Calderon, 2006 Journal of Applied Physics **100** 053907

[90] Z V Popović and A Milutinović 2006 Phys. Rev. B **73**, 155203

[91] L Sangaletti, S Dash, A Verdini, L Floreano, A Goldoni, G Drera, S Pagliara and A Morgante 2012 J. Phys.: Condens. Matter **24** 235502

[92] S Dash, M C Mozzati, P Galinetto, G Drera, S Pagliara and L Sangaletti to appear on J. Phys.: Conference series, SCES-2011, Cambridge

[93] S Dash and L Sangaletti in prepartion.

[94] A Fujimori, M Sacki, N Kimizuka, M Taniguchi and S Suga 1986 Physical Review B **34** 7318

[95] L Sangaletti, A Verdini, S Pagliara, G Drera, L Floreano, A Goldoni and A Morgante, 2010 Physical Review B **81** 245320

[96] L Ley, M Taniguchi, J Ghijsen, R L Johnson and A Fujimori, 1987 Phys. Rev. B **35** 2839

[97] T Mizokawa and A Fujimori, 1993 Physical Review B **48** 14150

[98] L Sangaletti, S Pagliara, I Dimitri, F Parmigiani, A Goldoni, L Floreano, A Morgante, V F Aguekian 2004 Surface Science **566-568 Part 1** 508514

[99] J B C Efrem D'sa, P A Bhobe, K R Prilkar, A Das, P S R Krishna, P R Sarode and R B Prabhu 2004 Pramana-Journal of Physics **63** 227-232